REPORT DOCUMENTATION PAGE	*Form Approved* *OMB No. 0704-0188*

The public reporting burden for this collection of information is estimated to average 1 hour per response, including the time for reviewing instructions, searching existing data sources, gathering and maintaining the data needed, and completing and reviewing the collection of information. Send comments regarding this burden estimate or any other aspect of this collection of information, including suggestions for reducing the burden, to Department of Defense, Washington Headquarters Services, Directorate for Information Operations and Reports (0704-0188), 1215 Jefferson Davis Highway, Suite 1204, Arlington, VA 22202-4302. Respondents should be aware that notwithstanding any other provision of law, no person shall be subject to any penalty for failing to comply with a collection of information if it does not display a currently valid OMB control number.
PLEASE DO NOT RETURN YOUR FORM TO THE ABOVE ADDRESS.

1. REPORT DATE *(DD-MM-YYYY)*	2. REPORT TYPE	3. DATES COVERED *(From - To)*
11-05-2011		

4. TITLE AND SUBTITLE	5a. CONTRACT NUMBER
Tunable Patch Antennas Using Microelectromechanical Systems	
	5b. GRANT NUMBER
	5c. PROGRAM ELEMENT NUMBER
6. AUTHOR(S)	5d. PROJECT NUMBER
Yec, Steven Christopher	
	5e. TASK NUMBER
	5f. WORK UNIT NUMBER

7. PERFORMING ORGANIZATION NAME(S) AND ADDRESS(ES)	8. PERFORMING ORGANIZATION REPORT NUMBER
9. SPONSORING/MONITORING AGENCY NAME(S) AND ADDRESS(ES)	10. SPONSOR/MONITOR'S ACRONYM(S)
U.S. Naval Academy Annapolis, MD 21402	
	11. SPONSOR/MONITOR'S REPORT NUMBER(S)
	Trident Scholar Report no. 403 (2011)

12. DISTRIBUTION/AVAILABILITY STATEMENT

This document has been approved for public release; its distribution is UNLIMITED

13. SUPPLEMENTARY NOTES

14. ABSTRACT

Patch antennas are enablers in wireless applications due to their manufacturability, conformability, low cost, and low weight. However, they have narrow bandwidths and fixed operating frequencies that limit their utility when frequency agility is critical. The solution is a tunable patch antenna that retains the desirable features of its fixed frequency counterparts. Patch antennas can be tuned without changes in geometry through loading with variable capacitors or inductors. These components must be small, compatible with antenna and integrated electronics processing, and electrically controlled. Microelectromechanical systems (MEMS) variable components have these characteristics and have been applied in reconfigurable patch antennas. Loading with MEMS capacitors is a more mature technology while the use of MEMS inductors is in its infancy. Antennas tuned with both MEMS variable inductors and capacitors in combination have not been reported. This research presents tunable patch antennas using MEMS variable inductors and capacitors co-fabricated in the same process.

15. SUBJECT TERMS

Microstrip antennas, patch antennas, radio frequency microelectromechanical systems, tunable circuits and devices

16. SECURITY CLASSIFICATION OF:			17. LIMITATION OF ABSTRACT	18. NUMBER OF PAGES	19a. NAME OF RESPONSIBLE PERSON
a. REPORT	b. ABSTRACT	c. THIS PAGE			
				69	19b. TELEPHONE NUMBER *(Include area code)*

Standard Form 298 (Rev. 8/98)
Prescribed by ANSI Std. Z39.18

U.S.N.A. --- Trident Scholar project report; no. 403 (2011)

Tunable Patch Antennas Using Microelectromechanical Systems

by

Midshipman 1/c Steven C. Yee
United States Naval Academy
Annapolis, Maryland

____
(signature)

Certification of Adviser(s) Approval

Associate Professor Deborah M. Mechtel
Electrical Engineering Department

____
(signature)

____
(date)

Associate Professor Samara L. Firebaugh
Electrical Engineering Department

____
(signature)

____
(date)

Office of Naval Research Distinguished Chair Harry K. Charles
Electrical Engineering Department

____
(signature)

____
(date)

Acceptance for the Trident Scholar Committee

Professor Carl E. Wick
Associate Director of Midshipman Research

____
(signature)

____
(date)

Abstract

Patch antennas are enablers in wireless applications due to their manufacturability, conformability, low cost, and low weight. However, they have narrow bandwidths and fixed operating frequencies that limit their utility when frequency agility is critical.

The solution is a tunable patch antenna that retains the desirable features of its fixed frequency counterparts. Patch antennas can be tuned without changes in geometry through loading with variable capacitors or inductors. These components must be small, compatible with antenna and integrated electronics processing, and electrically controlled.

Microelectromechanical systems (MEMS) variable components have these characteristics and have been applied in reconfigurable patch antennas. Loading with MEMS capacitors is a more mature technology while the use of MEMS inductors is in its infancy. Antennas tuned with both MEMS variable inductors and capacitors in combination have not been reported. This research presents tunable patch antennas using MEMS variable inductors and capacitors co-fabricated in the same process.

To prove the tuning concept, patch antennas were loaded with discrete inductors and capacitors and tested. The results demonstrated frequency shifts as wide as 1.71 GHz with little impact on antenna radiation patterns.

MEMS capacitors and inductors were designed and manufactured using the MetalMUMPS© process. The capacitor uses electrostatic control to vary the distance between parallel plates, altering device capacitance. The inductor features pre-deformed beams that buckle under thermally-actuated mechanical force. Change in loop area formed by the beams alters device inductance.

The MEMS were tested over an input voltage range from 0–100 V. A 5 GHz patch antenna incorporating the MEMS inductor as a variable load was designed and tested. Results were compared to those of the unloaded antenna and demonstrated an operating frequency shift of 810 MHz, a tunable range of 40 MHz for input voltages from 0–30 V, and a secondary 7.85 GHz resonant mode.

Keywords: Microstrip antennas, patch antennas, radio frequency microelectromechanical systems, tunable circuits and devices

Acknowledgements

I am grateful to the Naval Academy electrical engineering lab technicians Jerry Ballman, Erich Keyes, Bill Stanton, Daphi Jobe, Ken Walsh, Marcus Sydnor, and Mark Bergman not only for their support in equipment and parts acquisition, but also for their indispensable help in the maintenance and even construction of the laboratory facilities I have used for this project, particularly the microfabrication lab and anechoic chamber.

I also wish to express deep gratitude to Eldwin Dodson, Matiwos Kafel, Nicholas Nowicki, Lesly Piñol, and John Lehtonen at the Johns Hopkins Applied Physics Laboratory for their generous support in the critical fabrication and integration aspects of the project.

Thanks are due to Dr. Michelle Koul for allowing me to share the Wyco interferometer in the Naval Academy corrosion lab. Special recognition belongs to Dr. Chris Anderson for all his assistance in the testing phase of the project and particularly for allowing me to use the anechoic chamber without which none of this would be feasible.

Most importantly, I owe everything to Dr. Deborah Mechtel, Dr. Samara Firebaugh, and Dr. Harry Charles who not only provided me valuable guidance and motivation, but also allowed me the freedom to direct the project, leading to a truly invaluable independent research experience. I would also be remiss if I failed to mention the personal sacrifices made by Drs. Mechtel and Firebaugh, who consistently pushed and received last minute equipment shipments, even on the weekends. I could not imagine more dedicated or helpful advisers.

Lastly, I wish to thank my wonderful parents and Margaret Musick for their love, support, and understanding through the years and particularly through the course of the long, late, and weekend hours spent on this project.

Table of Contents

Abstract....1
Acknowledgements....2
Table of Contents....3
List of Figures....4
Antenna Theory....7
    Patch Antennas....7
    Feedlines and Impedance Matching....9
Proof of Concept....20
    Baseline Microstrip Antenna Design....20
    Loaded Microstrip Antenna Design....22
    Microstrip Antenna Fabrication....23
    Microstrip Antenna Testing....26
    Microstrip Antenna Data Analysis....30
Microelectromechanical Systems....31
    MEMS Variable Capacitor Design....32
    MEMS Variable Inductor Design....35
    MEMS Fabrication....38
    MEMS Device Testing....40
Integrated System....45
    MEMS Coplanar Waveguide Antenna Design....45
    Fabrication and Integration....46
    Testing and Analysis....48
Future Work....52
Conclusions....54
References....55
Appendix A: Patch Antenna Dimension Calculation....56
Appendix B: Microstrip Line Width Calculation....60
Appendix C: MetalMUMPs [16]....61
Appendix D: MetalMUMPs Mask Layout....69

List of Figures

Figure 1: Conceptual diagram of a patch antenna 7
Figure 2: Side view of patch antenna with electric field at resonance 8
Figure 3: Return loss (S11) of fabricated 5.53 GHz patch antenna....8
Figure 4: Radiation pattern of fabricated 5.53 GHz patch antenna 9
Figure 5: (a) Capacitor voltage and current waveforms (b) inductor voltage and current waveforms 10
Figure 6: Patch antenna impedance model 11
Figure 7: Theoretical resistance (top) and reactance (bottom) of 9 GHz patch antenna 12
Figure 8: Transmission line circuit model....13
Figure 9: Diagram of microstrip transmission line....14
Figure 10: Diagram of coplanar waveguide transmission line 15
Figure 11: Diagram of patch antenna with quarter wavelength transformer....16
Figure 12: Diagram of patch antenna with inset feed....17
Figure 13: Diagram of patch antenna with capacitive loading stub 18
Figure 14: Mask layout for baseline 5.5 GHz patch antenna 22
Figure 15: Mask layout for loaded 5.5 GHz patch antenna....22
Figure 16: Simulated return loss of loaded and unloaded 5.5 GHz patch antennas 23
Figure 17: Spin-coater and hot plate used for circuit board fabrication....24
Figure 18: UV radiation exposure device used in circuit board fabrication....24
Figure 19: Baseline 5.5 GHz patch antenna 25
Figure 20: 5.5 GHz patch antenna with discrete reactive load....26
Figure 21: Naval Academy anechoic chamber....26
Figure 22: Measured return loss of loaded and unloaded 5.5 GHz patch antennas 27
Figure 23: Diagram of radiation pattern test setup....28
Figure 24: Radiation pattern of unloaded patch antenna at 5.54 GHz 28
Figure 25: Radiation pattern of 6.5 nH loaded patch antenna at 6.36 GHz....29
Figure 26: Radiation pattern of 7.4 nH loaded patch antenna at 5.99 GHz....29
Figure 27: Radiation pattern of 6.8 pF loaded patch antenna at 5.47 GHz 30
Figure 28: MetalMUMPs process summary [16]....31
Figure 29: Diagram of MEMS capacitor, isometric view 32
Figure 30: Diagram of MEMS capacitor, side view....33
Figure 31: Diagram of MEMS capacitor, close up side view 33
Figure 32: Diagram of MEMS capacitor showing mechanical restoring force....34
Figure 33: Diagram of MEMS inductor, top view 35
Figure 34: Simulation of inductor beams under 0 N lateral force....36
Figure 35: Simulation of inductor beams under 25 mN lateral force....36
Figure 36: Diagram of thermal actuator 37
Figure 37: Diagram of electrically isolated, mechanically coupled bridge, side view....38
Figure 38: Photograph of MEMS variable capacitor....39
Figure 39: Photograph of MEMS variable inductor....39
Figure 40: (a) MEMS variable capacitor mounted on test circuit (b) close up view 40
Figure 41: MEMS device test setup 41
Figure 42: Measured capacitance of MEMS variable capacitor with trendlines....41
Figure 43: Measured inductance of MEMS variable inductor 42
Figure 44: (a) Wyko rendering of bridge structure at 0 V and (b) at a 50 V bias voltage....43
Figure 45: Wyko 3-D rendering of MEMS inductor actuator array....44
Figure 46: Mask layouts for 5 GHz baseline CPW antenna, (left) feed, (right) antenna 45
Figure 47: Mask layouts for MEMS-tuned antenna, (top left) feed, (top right) antenna, (bottom) control lines 46
Figure 48: Diagram of (a) back and (b) front of MEMS-tuned antenna 47
Figure 49: Photograph of front (left) and back (right) of fabricated MEMS-tuned antenna....48
Figure 50: Measured return loss of CPW-fed antennas, 4.5-6.5 GHz....48
Figure 51: Measured return loss of CPW-fed antennas, 7-8 GHz....49

Figure 52: Measured return loss of MEMS-tuned antenna after device burn out 50
Figure 53: Radiation patterns of baseline CPW antenna at (a) 5.085 GHz, (b) 5.890 GHz, and (c) 7.850 GHz 51
Figure 54: Radiation patterns of MEMS-tuned antenna at (a) 5.085 GHz, (b) 5.890 GHz, and (c) 7.850 GHz 51
Figure 55: L network circuit diagram 52
Figure 56: Simulated return loss of rectangular patch antenna loaded with variable L network 52
Figure 57: Circuit diagram of Π network load 53
Figure 58: Simulated return loss rectangular patch antenna loaded with variable Π network 53

Introduction

Motivation

Patch antennas are planar microstrip structures uniquely suited to wireless applications where mass and profile are critical. Due to their low weight, conformability, and easy fabrication, patch antennas deliver wireless capability to aircraft and spacecraft without the drag or mass of other antenna types and offer lightweight, rugged solutions for tactical soldier communication and navigation systems [1].

However, such resonant antennas typically suffer from narrow bandwidths and a fixed operating frequency, which limits their usefulness in applications where frequency agility is critical [1]. Patch antennas with a tunable operating frequency can overcome this limitation, allowing a single antenna design to serve a system requiring access to multiple frequencies [2]. Such reconfigurable designs better meet the demands of modern wireless applications from smart phones to cognitive radios.

Recent reconfigurable planar antenna designs have capitalized on the low power, small geometries, and good performance characteristics of microelectromechanical systems (MEMS) to achieve a tunable operating frequency. MEMS can serve as switches, phase shifters, and tunable reactive elements with low power consumption, low insertion loss, and high linearity [3]. Discrete frequency tuning has been achieved with MEMS switches that reconfigure antenna geometries [3], and continuous frequency tuning has been achieved by loading antenna structures with MEMS variable capacitors. To date, such designs for reconfigurable patch antennas have achieved frequency shifts as wide as 300 MHz in the 15–16 GHz [4], 5–6 GHz, and 1.5–2.5 GHz frequency regions [5] and 1 GHz in the 10–12 and 7–8 GHz frequency regions [6].

Although loading antenna structures with MEMS variable capacitors is a well-documented method in reconfigurable antenna design [4], MEMS variable inductors have not received the same attention in that role even though the application principle is similar and prior study of such devices is considerable [7]–[10]. This research intends to enhance the art of reconfigurable patch antenna design by exploring the use of MEMS variable inductors as reactive loads both individually and in combination with MEMS variable capacitors in variable matching networks.

Goals

The research goal was to demonstrate a proof of concept patch antenna tuning system using MEMS variable inductors and capacitors. The operating frequency of the antenna should shift under applied voltage to a MEMS variable reactive component with minimal impact on the antenna’s radiation pattern. Due to fabrication and testing equipment limitations, the antenna target frequency range was 4–6 GHz, and the MEMS components were limited to multi-user MEMS processes.

Antenna Theory

Patch Antennas

Patch antennas are a type of resonant antenna introduced in the 1950s and are an outgrowth of microstrip transmission line development [11]. Generally, patch antennas consist of a planar metal radiator parallel to and separated from a metal ground plane by a dielectric substrate, typically a high frequency circuit board material. A diagram of a rectangular patch antenna is shown in Figure 1.

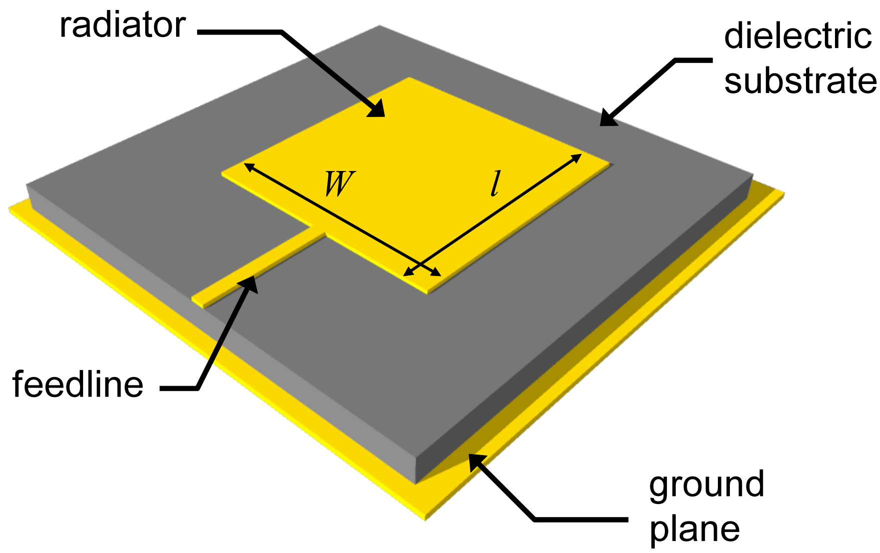

Figure 1: Conceptual diagram of a patch antenna

Patch antennas may have a variety of shapes and radiate from edge discontinuities. The rectangular patch antenna has the simplest geometry, resonating when l as shown in Figure 1 is roughly half a wavelength λ. Wavelength λ is related to frequency f by the electromagnetic wave speed of propagation U as shown in Equation 1 below.

$$U = f\lambda \tag{1}$$

The electric field, which propagates in the direction of the feedline between the antenna and underlying ground plane, undergoes a 180° phase shift over a half wavelength segment of transmission line. This effect results in an electromagnetic wave radiating from two slots formed by the edges of the antenna and the ground plane in a direction normal to the plane of the antenna [1]. A side view of a patch antenna displaying the electric field at resonance is shown in Figure 2.

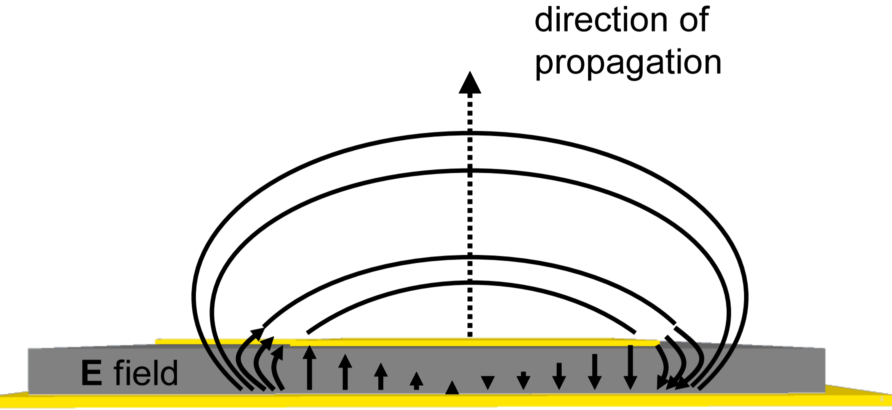

Figure 2: Side view of patch antenna with electric field at resonance

Antenna performance over frequency *f* can be expressed as either a voltage standing wave ratio (VSWR) or as return loss S11, which is also referred to as the reflection coefficient measured in decibels (dB). The lower the S11 of an antenna at a particular frequency, the better it resonates energy at that frequency into free space. A graph of the measured return loss of a 5.5 GHz patch antenna fabricated for this project is shown below as Figure 3. Note that at 5.53 GHz, the antenna achieves its best performance with a return loss of -21.5 dB. This very slight offset (<0.6%) in the resonant frequency of the fabricated antenna is a testament to the design process and the holding of key dimensions during fabrication.

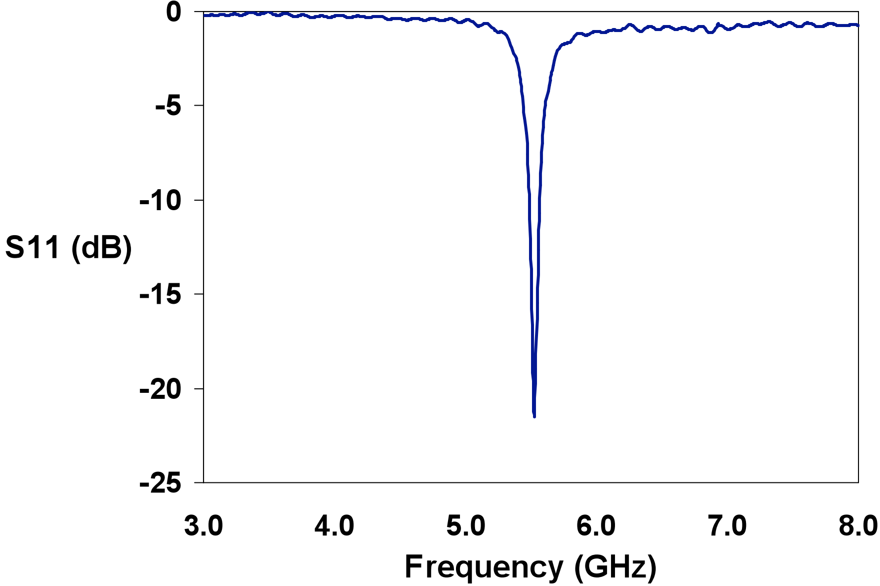

Figure 3: Return loss (S11) of fabricated 5.53 GHz patch antenna

Bandwidth is the range of frequencies relative to the center frequency over which an antenna can operate at low return loss (< -10dB), which is considered the maximum allowable loss for useful performance [12]. Typical patch antenna bandwidth is between 1% and 5% of the resonant frequency and is dependent on the substrate height h and dielectric constant ε_r. The patch

antenna whose return loss is plotted in Figure 3 has a bandwidth of 70 MHz or 1.3% of the 5.53 GHz resonant frequency. An empirical formula [11] for patch antenna bandwidth B is given below as Equation 2.

$$B = 3.77 \frac{\varepsilon_r - 1}{\varepsilon_r^2} \frac{W}{l} \frac{h}{\lambda} \, , \; \frac{h}{\lambda} \ll 1 \tag{2}$$

Although bandwidth increases with increased substrate height, side lobe strength in the antenna's radiation pattern also increases. The measured radiation pattern of the fabricated 5.53 GHz antenna discussed previously is shown below as Figure 4.

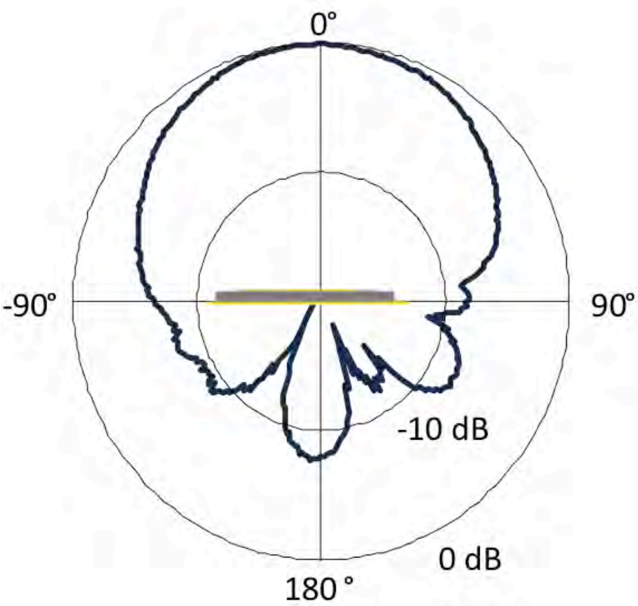

Figure 4: Radiation pattern of fabricated 5.53 GHz patch antenna

The principle beam or main lobe of an antenna is in the direction where the antenna radiates the most power. The main lobe in Figure 4 is centered approximately at 0 degrees. The angular limits where antenna power falls to half the maximum power define the beamwidth of the antenna [11]. Power radiated by an antenna in other directions represents side lobes that may be undesirable depending on the application. In applications such as radar, minimizing side lobes so that antenna energy is highly directed is critical.

Feedlines and Impedance Matching

Matching antenna input impedance to the characteristic impedance of a transmission feedline is critical to avoid wave reflection that reduces performance and can even damage transmission circuits. All antennas can be modeled as a load of a particular impedance Z, the ratio of the AC voltage to the AC current measured in ohms. To achieve optimal performance, antenna impedance must be matched to the characteristic impedance Z_0 of receiving or transmission circuits. Impedance is a frequency dependent quantity expressed in units of ohms. It is represented by a complex number with a real component known as resistance R and an imaginary component known as reactance X as shown in rectangular form below in Equation 3 [13].

$$Z(f) = R(f) + jX(f)\Omega \tag{3}$$

Reactance *X* is the impedance due to capacitance *C* or inductance *L* that cause voltage to lag current or current to lag voltage, respectively. In capacitors, flowing current that builds up charge on capacitor electrodes leads voltage that is proportional to electrode charge. In inductors, current lags voltage because the structure resists rapid changes in current as expressed in Lenz's Law [13]. Time domain graphs of voltage and current waveforms in capacitors and inductors are shown below in Figure 5. Equation 4 below relates capacitance C and inductance L to reactance *X*.

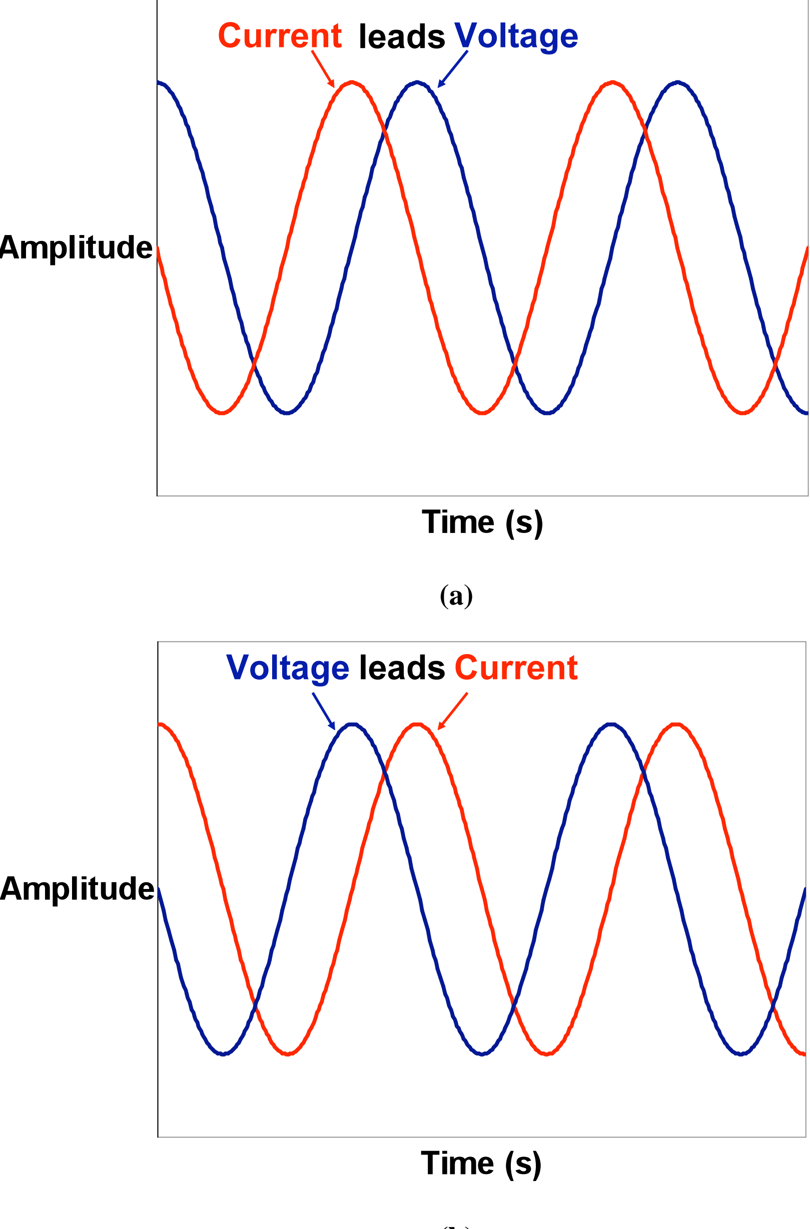

Figure 5: (a) Capacitor voltage and current waveforms (b) inductor voltage and current waveforms

$$X(f) = 2\pi f \cdot L - \frac{1}{2\pi f \cdot C} \tag{4}$$

Patch antenna impedance can be modeled [1] as two radiating slots of resistance R_x and capacitance C_x connected in parallel across a segment of transmission line of length l equal to about half a wavelength as shown below in Figure 6.

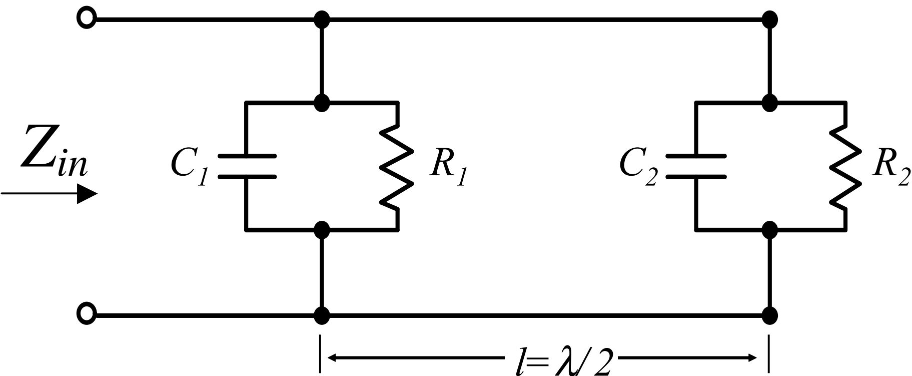

Figure 6: Patch antenna impedance model

When viewed from the antenna input at resonance, the capacitance of the slot farthest from the feedline undergoes a 180° phase shift as it is translated across the half wavelength transmission line and can be represented by an inductance L_2. At resonance, the reactance due to inductance L_2 balances the reactance due to the capacitance C_1, resulting in a purely real antenna input impedance Z as shown below in Equations 5, 6, and 7 [1].

$$L_2 = \frac{1}{(2\pi f_{res})^2 C_1} \tag{5}$$

$$X(f_{res}) = 2\pi f_{res} \cdot L_2 - \frac{1}{2\pi f_{res} \cdot C_1} = 0 \tag{6}$$

$$Z(f_{res}) = R(f_{res}) + jX(f_{res}) = R(f_{res}) \tag{7}$$

At resonance, the input resistance R is typically between 100 and 400 Ω. An empirical formula characterizing edge-fed rectangular patch antenna resonant impedance $Z(f_{res})$ as a function of the length l, width W, and dielectric constant ε_r, given by Stutzman [11] is shown below as Equation 8.

$$Z(f_{res}) = R(f_{res}) = 90 \frac{\varepsilon_r^2}{\varepsilon_r - 1} \left(\frac{l}{W} \right)^2 \Omega \tag{8}$$

A graph of the theoretical input impedance of an 8.955 GHz patch antenna over frequency is shown below in Figure 7 [1]. Note that at the antenna's resonant frequency of 8.955 GHz, resistance is at a maximum of 120 Ω and that reactance is minimal. When reactance is positive, the antenna impedance can be characterized as inductive. When reactance is negative, the antenna impedance is capacitive.

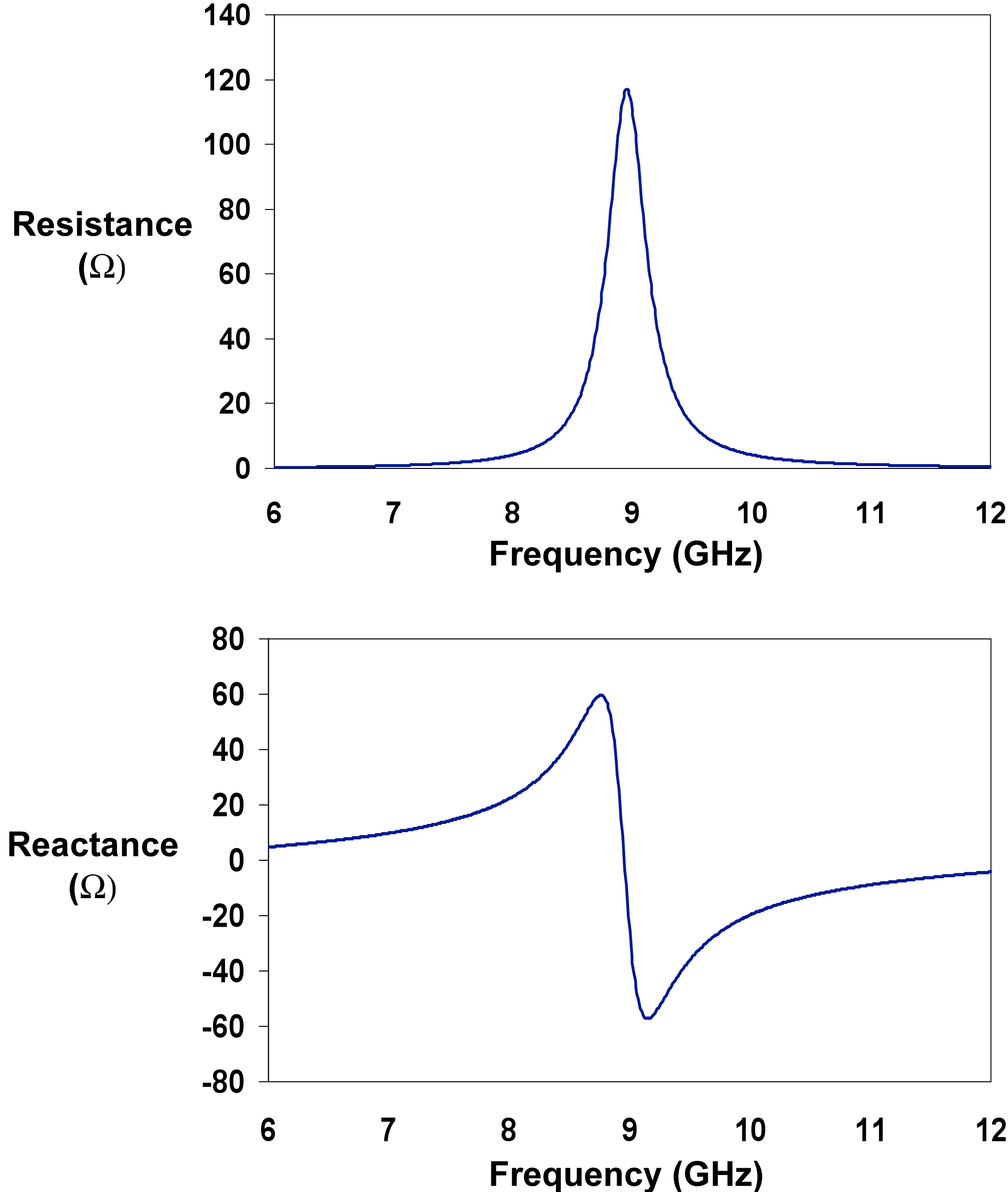

Figure 7: Theoretical resistance (top) and reactance (bottom) of 9 GHz patch antenna

A transmission line is used as the feedline for the patch antenna illustrated in Figure 1. The characteristic impedance Z_0 of a transverse electromagnetic (TEM) transmission line is dependent on transmission line geometry and materials. TEM transmission lines may be modeled

using the lumped element circuit model shown below in Figure 8 with resistance *R*, admittance *G*, inductance *L*, and capacitance *C* [14]. Admittance *G* is the inverse of resistance *R*.

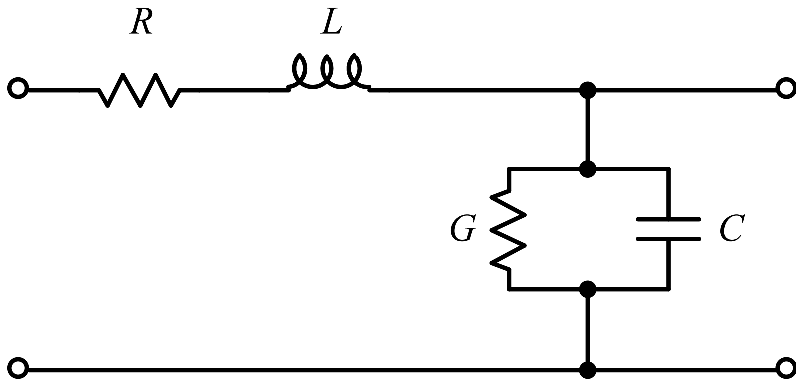

Figure 8: Transmission line circuit model

For simplicity, most transmission lines are modeled as lossless lines where *R* and *G* are negligible. This results in a characteristic impedance Z_0 equal to the square root of the inductance *L* to capacitance *C* ratio of a transmission line as shown below in Equation 9 [14]. Most transmission lines used to feed patch antennas have a characteristic impedance of 50 Ω.

$$Z_0 = \sqrt{\frac{L}{C}} \quad (9)$$

The two most common transmission line structures used to feed patch antennas are microstrip lines and coplanar waveguides. Microstrip lines are similar to and easily integrated with patch antennas. They consist of a length of thin metal parallel to and separated from a ground plane by a dielectric substrate. Electric fields are guided by the metal trace and underlying ground plane mostly within the dielectric substrate [14]. A diagram of a microstrip transmission line is shown below as Figure 9.

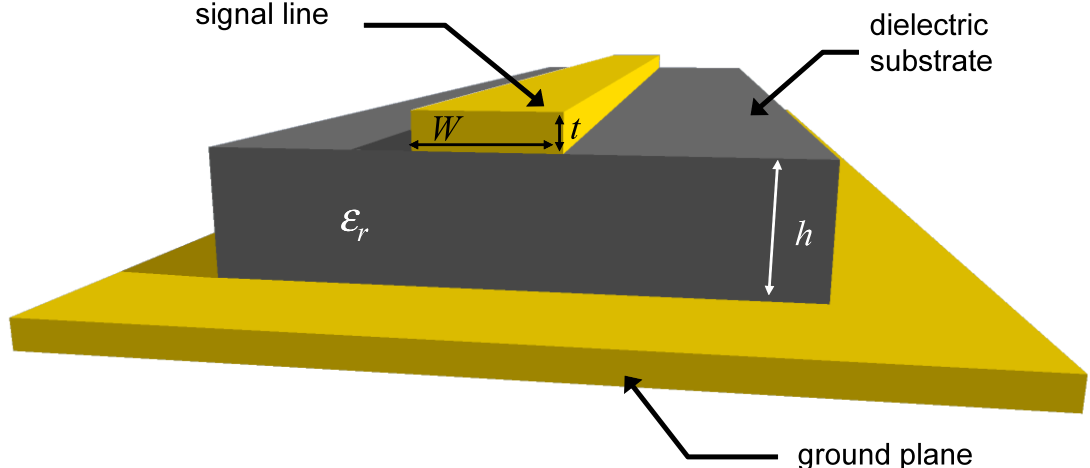

Figure 9: Diagram of microstrip transmission line

The characteristic impedance Z_0 of microstrip lines is a function of substrate height h, metal layer thickness t, dielectric constant ε_r, and the strip width W and can be determined with the empirical formulas [14] shown as Equations 10–12.

$$Z_0 = \frac{120\pi}{2\pi\sqrt{2(\varepsilon_e+1)}} \ln\left\{1+\frac{4h}{W'}\left[\frac{14+\frac{8}{\varepsilon_e}}{11}\cdot\frac{4h}{W'}+\sqrt{\left(\frac{14+\frac{8}{\varepsilon_e}}{11}\right)^2\left(\frac{4h}{W'}\right)^2+\left(\frac{1+\frac{1}{\varepsilon_e}}{2}\right)\pi^2}\right]\right\}\Omega \tag{10}$$

$$\varepsilon_e = \begin{cases} \text{if } W/h \le 1, & \frac{\varepsilon_r+1}{2}+\frac{\varepsilon_r-1}{2}\left[\left(1+\frac{12h}{W}\right)^{-0.5}+0.04\left(1-\frac{W}{h}\right)^2\right] \\ \text{if } W/h \ge 1, & \frac{\varepsilon_r+1}{2}+\frac{\varepsilon_r-1}{2}\left(1+\frac{12h}{W}\right)^{-0.5} \end{cases} \tag{11}$$

$$W' = W + t\cdot\frac{1}{\pi}\cdot\left(\frac{1+1/\varepsilon_r}{2}\right)\ln\left[\frac{4e}{\sqrt{(t/h)^2+\left(\frac{1/\pi}{W/t+1.1}\right)^2}}\right] \tag{12}$$

Another type of transmission line structure is coplanar waveguide (CPW). CPW consists of a ground plane coplanar with the signal trace as shown in Figure 10 below. The characteristic impedance Z_0 of CPW structures is a function of the dielectric constant ε_r, metal layer thickness t, substrate height h, signal line width a, and the total gap and signal width b. Formulas for

determining the characteristic impedance of CPW structures are given below as Equations 13–19 [14]. Note that the function *K(k)* denotes the complete elliptic integral of the first kind.

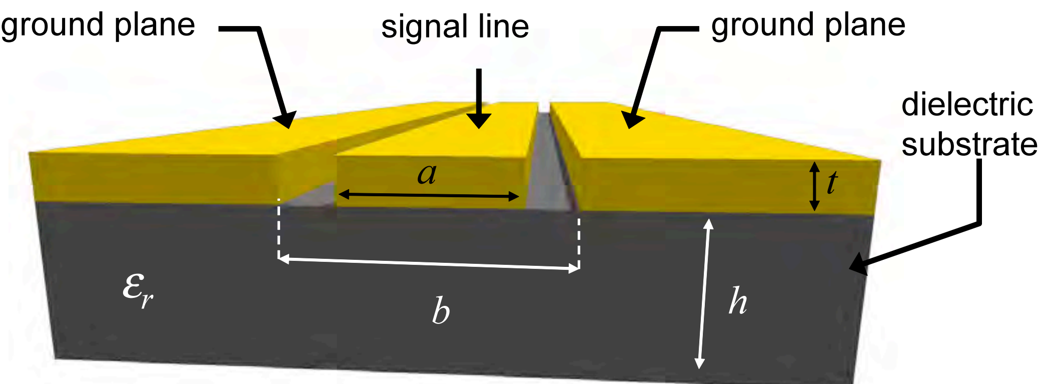

Figure 10: Diagram of coplanar waveguide transmission line

$$Z_0 = \frac{30\pi}{\sqrt{\varepsilon_{e,t}}} \frac{K(k_t')}{K(k_t)} \tag{13}$$

$$\varepsilon_{e,t} = \varepsilon_e - \frac{\varepsilon_e - 1}{\frac{(b-a)/2}{0.7t} \frac{K(k)}{K'(k)} + 1} \tag{14}$$

$$\varepsilon_e = 1 + \frac{\varepsilon_r - 1}{2} \frac{K(k')K(k_1)}{K(k)K(k_1')} \tag{15}$$

$$k = \frac{a}{b} \qquad k_t = \frac{a_t}{b_t} \qquad k_1 = \frac{\sinh\left(\frac{\pi a_t}{4h}\right)}{\sinh\left(\frac{\pi b_t}{4h}\right)} \tag{16}$$

$$k_x' = \sqrt{1 - k_x^2} \tag{17}$$

$$a_t = a + \frac{1.25t}{\pi}\left[1 + \ln\left(\frac{4\pi a}{t}\right)\right] \tag{18}$$

$$b_t = b - \frac{1.25t}{\pi}\left[1 + \ln\left(\frac{4\pi a}{t}\right)\right] \tag{19}$$

Unlike microstrip structures, CPWs require only one metallization layer and can change trace width while maintaining constant characteristic impedance by varying the gap width. Also, CPW

feeds allow microstrip antennas to conceal the antenna feed network on the reverse side of the substrate from the antenna. This can be advantageous when sensitive electronic components are involved. However, CPW feeds are not as easily integrated with patch antenna structures.

To ensure the strongest radiated signal, a number of different methods can be used to match patch antenna impedances, which are typically between 100 and 400 Ω [11], to the characteristic 50 Ω impedance of transmission line structures. The first method is to solve for the patch width W given the patch length l using Equation 6. However, this method can be undesirable when space is at a premium.

Another method is to use a quarter wavelength transformer, which is a segment of transmission line one quarter wavelength long with characteristic impedance Z_q. Z_q is equal to the square root of the product of the edge-fed antenna input impedance Z and the desired impedance Z_0 as viewed from the input [11]. A diagram of a microstrip-fed patch antenna with a quarter wavelength transformer is shown in Figure 11. Equation 20 summarizes the calculation of the required characteristic impedance for a quarter wavelength transformer [11].

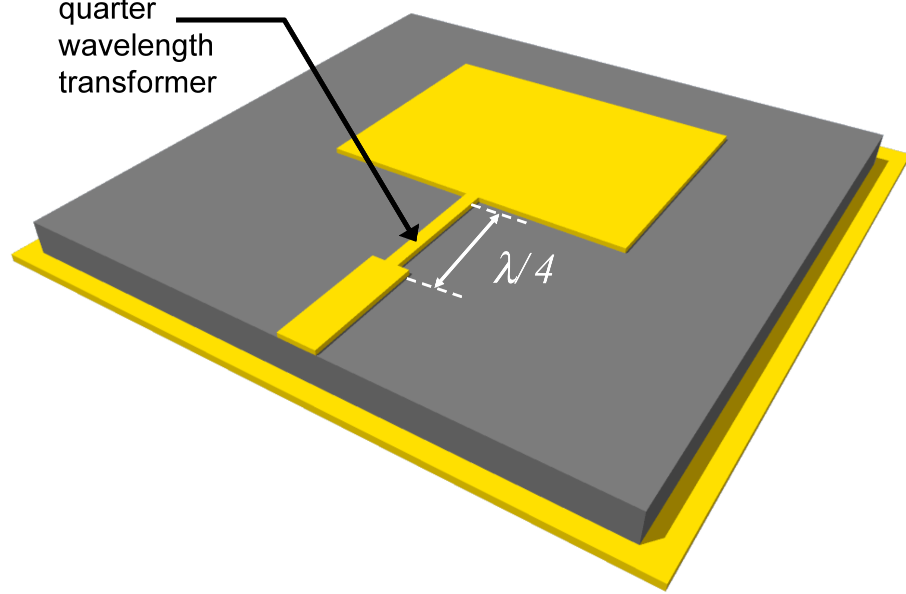

Figure 11: Diagram of patch antenna with quarter wavelength transformer

$$Z_q = \sqrt{Z \cdot Z_0} \tag{20}$$

Another method for matching antenna and transmission line impedances is to use an inset feed point as shown below in Figure 12. Insetting the feed point by distance Δx alters the antenna input impedance according to Equation 21 below [1]. Inset feeds can be used with both microstrip and coplanar transmission lines as long as the coplanar line is on a separate layer from the antenna.

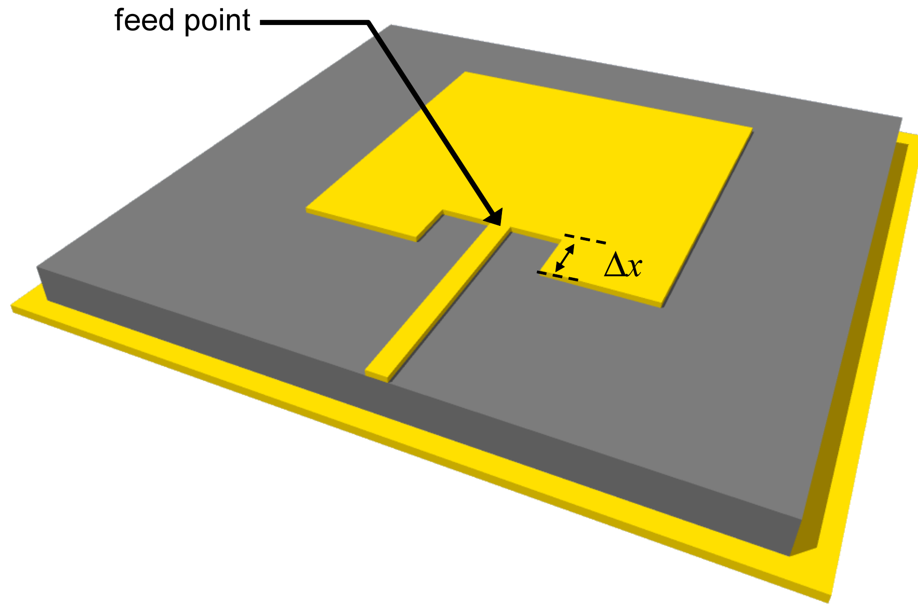

Figure 12: Diagram of patch antenna with inset feed

$$Z(\Delta x) = Z(\Delta x = 0) \cdot \cos^2\left(\frac{\pi \cdot \Delta x}{L}\right) \quad (21)$$

Finally, an antenna-transmission line impedance match can be made using a reactive load on the feedline at a distance from the input such that the resultant input impedance appears purely real. This is the simplest impedance matching method and has traditionally been executed using tuning stubs, small open-circuited or short-circuited segments of transmission line that serve as capacitors or inductors [11]. Examples of this impedance matching method are shown below in Figure 13. The equation governing the equivalent input impedance of a load at a distance d from the input is shown below as a function of the characteristic impedance Z_0 of the transmission feedline, the load impedance Z_L, which is the input impedance of the antenna, and wavelength λ in Equation 22 [15]. The stub is used to cancel out the reactive part of the calculated input impedance in Equation 22.

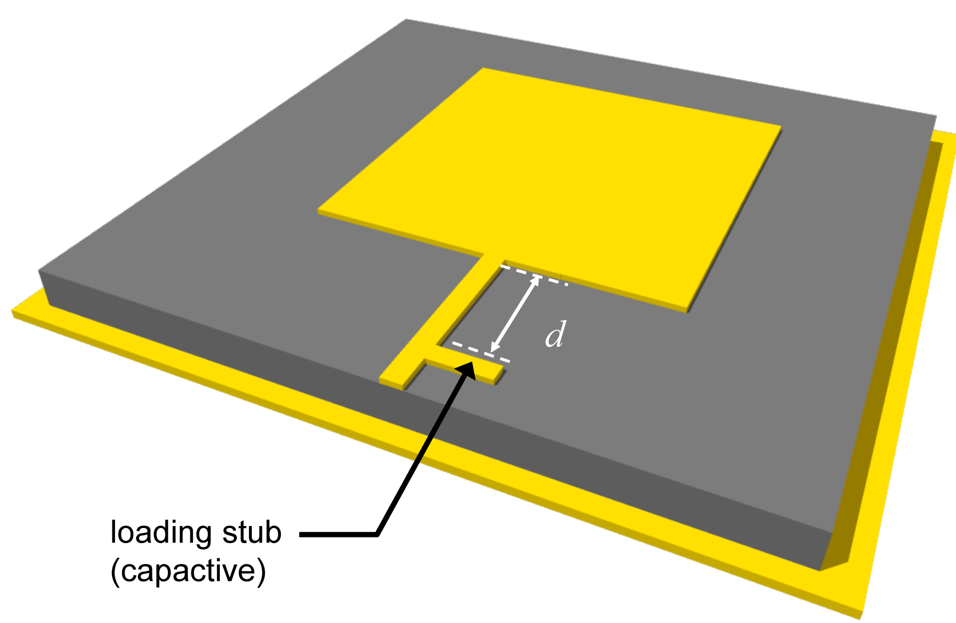

Figure 13: Diagram of patch antenna with capacitive loading stub

$$Z_{in} = Z_0 \left[\frac{Z_L + jZ_0 \tan\left(\left(\frac{2\pi}{\lambda}\right)d\right)}{Z_0 + jZ_L \tan\left(\left(\frac{2\pi}{\lambda}\right)d\right)} \right] \Omega \tag{22}$$

Tuning Concepts

Impedance matching using reactive loading is the fundamental principle behind the patch antenna tuning method proposed in this research. By loading an antenna with a variable inductance or capacitance rather than a static reactance, an antenna can be tuned by matching its impedance at frequencies other than its resonant frequency to the feedline, minimizing reflection and mitigating the bandwidth limitation of patch antennas [2].

As shown in Figure 7, the impedance of a patch antenna varies over frequency with resonance occurring at the frequency where resistance is at a maximum and reactance is at a minimum. At other frequencies, the antenna can be considered an inductive or capacitive load. Using Equation 22 to calculate the input impedance Z_{in} at some distance d from the load along a feedline and Equation 4 to calculate reactance, one can solve for the required inductance L or capacitance C required at that position.

As a simplified theoretical example, consider a patch antenna with a 9 GHz resonant frequency that one desires to tune to 9.25 GHz and 9.75 GHz. Modeling the antenna as a load as shown in Figure 11, the antenna impedance Z_a is equal to $40 - j15\ \Omega$ at 9.25 GHz and $10 - j10\ \Omega$ at 9.75 GHz. Using Equation 22, one calculates that the input impedance Z_{in} seen from a distance of 19.4 mm from the antenna along a 50 Ω transmission line is $38.4548 - j13.38\ \Omega$ at 9.25 GHz and $9.77 - j6.57\ \Omega$ at 9.75 GHz.

At this position, an inductor with reactance X_C is desired that will offset the capacitive reactances of the antenna. Using Equation 4, one calculates that to offset $-j13.38\ \Omega$ at 9.25 GHz, an inductance of 0.23 nH is required. Using the same process, one calculates that to offset $-j6.57\ \Omega$ at 9.75 GHz, an inductance of 0.11 nH is required. Using a variable inductor with an inductance range between 0.1 and 0.25 nH as a controllable load 19.4 mm away from the antenna edge, the described antenna can be tuned between 9.25 and 9.75 GHz, assuming that antenna reactance is relatively linear with respect to frequency from 9.25 to 9.75 GHz.

Although this method of antenna tuning has been achieved using variable capacitors, little work has been done on variable inductors for this application. The research presented here is intended to validate the described tuning principle and furthermore prove that variable inductors can be used to tune patch antennas.

Proof of Concept

To demonstrate the concept of antenna tuning using variable reactive loads, a 5.5 GHz microstrip-fed rectangular patch antenna was designed and loaded with different surface mount inductors and capacitors. The return losses of the various antennas were then tested using a network analyzer.

Baseline Microstrip Antenna Design

The baseline antenna was designed for ULTRALAM® 2000 substrate with 1-oz. electrodeposited copper metallization layers, a material chosen for its mechanical strength and low dielectric constant. A microstrip transmission line was chosen for simplicity of integration with a patch antenna. The design process followed well-known equations outlined by Balanis [1].

First, a practical antenna width W was determined using Equation 23 below [1] where f_{res} is the desired unloaded resonant frequency, c is the free-space velocity of light, and ε_r is the dielectric constant of ULTRALAM® 2000, which is between 2.4 and 2.6.

$$W = \frac{c}{2 f_{res}} \sqrt{\frac{2}{\varepsilon_r + 1}} \tag{23}$$

Next, the effective dielectric constant ε_e was calculated using Equation 11, which was introduced earlier as the effective dielectric constant for a microstrip transmission line. The equation is repeated here for convenience [1]. An effective dielectric constant is used rather than the nominal dielectric constant because the electric field guided by microstrip structures travel both in the substrate and in the air. The effective dielectric constant is used to model the microstrip structure as if it were embedded in a single dielectric for simplicity [14].

$$\varepsilon_e = \begin{cases} \text{if } W/h \le 1, & \dfrac{\varepsilon_r + 1}{2} + \dfrac{\varepsilon_r - 1}{2}\left[\left(1 + \dfrac{12h}{W}\right)^{-0.5} + 0.04\left(1 - \dfrac{W}{h}\right)^2\right] \\ \text{if } W/h \ge 1, & \dfrac{\varepsilon_r + 1}{2} + \dfrac{\varepsilon_r - 1}{2}\left(1 + \dfrac{12h}{W}\right)^{-0.5} \end{cases} \tag{11}$$

After determining the effective dielectric constant, the fringing length Δl was calculated using Equation 24 [1]. This fringing length accounts for the fringing of the electric field at the radiating slots of a rectangular patch antenna. Note that in Figure 2 the electric field length extends beyond the physical geometric length of the antenna. The fringing length Δl is a function of substrate height h, effective dielectric constant ε_e, and antenna width W [1].

$$\Delta l = 0.412h \frac{(\varepsilon_e + 0.3)\left(\frac{W}{h} + 0.264\right)}{(\varepsilon_e - 0.258)\left(\frac{W}{h} + 0.8\right)} \tag{24}$$

Lastly, the geometric length of the patch antenna was determined using Equation 25 below where μ_0 and ε_0 are the permeability and permittivity of free space, respectively, f_{res} is the desired unloaded resonant frequency, and ε_e is the effective dielectric constant. The result is that the length l of the patch antenna is just under half the wavelength of the desired resonant frequency [1].

$$l = \frac{1}{2 f_{res} \sqrt{\varepsilon_e} \sqrt{\mu_0 \varepsilon_0}} - 2\Delta l \tag{25}$$

To aid in the design process a MATLAB script was written to solve for patch antenna dimensions given desired resonant frequency and substrate parameters. The code is provided as an appendix to this report. For a resonant frequency of 5.5 GHz, a nominal dielectric constant of 2.5, a metallization thickness of 35.56 μm, and a substrate height of 0.762 mm, the calculated dimensions for the patch antenna were 16.91 mm in length and 20.62 mm in width. The antenna input impedance at its edge was calculated to be 252.27 Ω using Equation 8.

In order to further refine the patch antenna design, the geometries derived from Equations 11, 23–25 were used as initial parameters for a computer model of the antenna using Sonnet™ High Frequency Electromagnetic Software. Using length and width as geometric parameters, an optimization analysis was run using Sonnet™, the resulting patch antenna dimensions were 16.81 mm in length and 20.62 mm in width. The simulated input impedance of 251.1 – j6.16E-12 Ω closely matched the impedance calculated using Equation 8 and confirmed that at resonance, input reactance is negligible.

To match the 251.1 Ω, 5.5 GHz antenna to a 50 Ω feedline at resonance, a quarter wavelength transformer was incorporated into the design. Using Equation 20, the required quarter wavelength transformer impedance was calculated to be 112 Ω.

Finally, using ULTRALAM® 2000 substrate parameters and Equations 10–12, the widths of 50 Ω and 112 Ω microstrip lines were calculated using a MATLAB script included as an appendix to this report. The calculated parameters were a 50 Ω microstrip line width of 2.24 mm and a quarter wavelength transformer width of 609.6 μm and length of 8.85 mm. The results of the theoretical calculations were used as initial inputs to optimization analyses using Sonnet™. After software optimization, the final transmission line parameters remained unchanged except that the quarter wavelength transformer width was decreased to 508 μm. The mask layout for the baseline antenna is shown below as Figure 14.

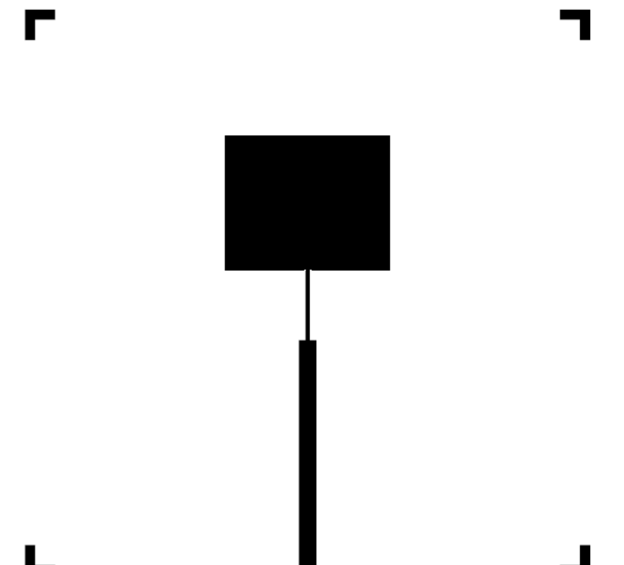

Figure 14: Mask layout for baseline 5.5 GHz patch antenna

Loaded Microstrip Antenna Design

In order to introduce reactive loads onto the previously described antenna, a landing pad for surface mount components was added to the baseline design at a distance 17.7 mm from the end of the quarter wavelength transformer using the input impedance as seen from the end of the quarter wavelength transformer as the load impedance. This distance was chosen not as an optimization but as an arbitrary position from which to test various reactive loads. The two symmetrical pads were designed to be 508 μm by 737 μm with a gap of 317.5 μm between them in order to accommodate 0402 size surface mount capacitors and 0302 size surface mount inductors. The mask layout for the loaded microstrip antenna is shown below as Figure 15.

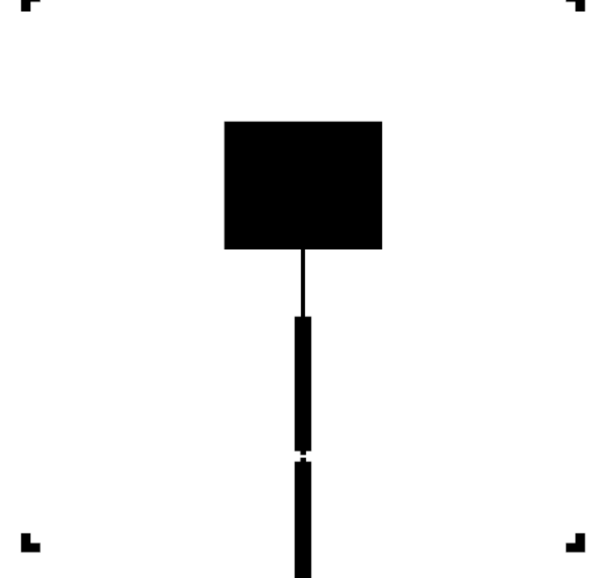

Figure 15: Mask layout for loaded 5.5 GHz patch antenna

Simulations using Sonnet™ for the layout in Figure 15 were conducted using the ideal component feature of the software, which models ideal passive elements within the geometry-driven electromagnetic model of the layout. Using a simulation parameter sweep of ideal inductor and ideal capacitor models, 0.67 nH, 6.5 nH, and 7.4 nH surface mount inductors and 1 pF, 2.2 pF, and 6.8 pF surface mount capacitors were chosen as loads. The simulated return losses for antennas loaded with 6.5 nH, 7.4 nH, and 6.8 pF components are shown below in Figure 16.

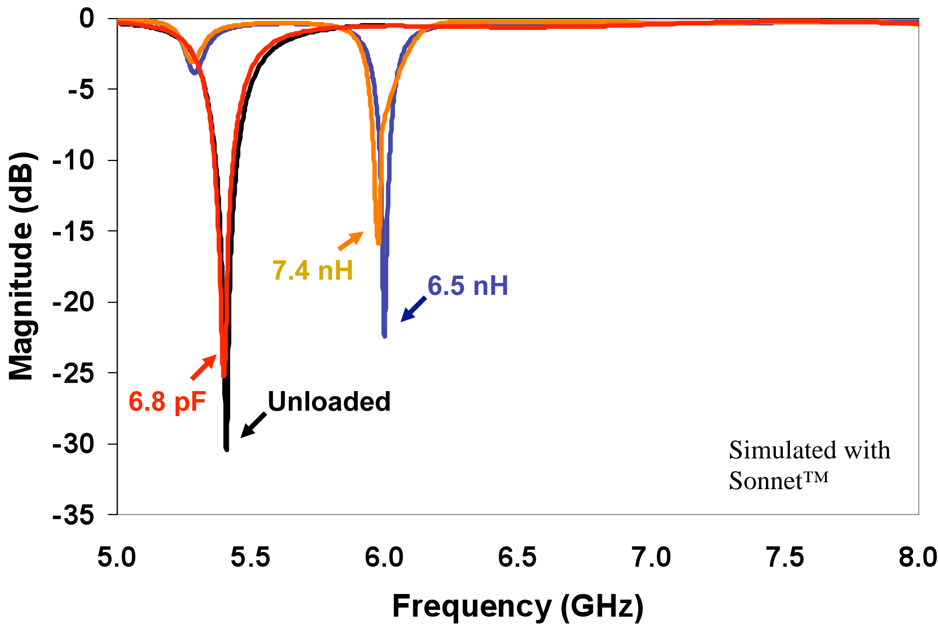

Figure 16: Simulated return loss of loaded and unloaded 5.5 GHz patch antennas

In Figure 16, simulated frequency shifts up to 6 GHz are shown with components of inductances around 7 nH. Figure 14 also demonstrates that at this particular distance, capacitive components are not as effective as inductive ones for tuning the antenna operating frequency. This is a function of the antenna impedance and the chosen distance between the reactive component and the input of the antenna's quarter wavelength transformer.

Microstrip Antenna Fabrication

Both the baseline and loaded microstrip antenna designs described previously were fabricated using a circuit board fabrication process in the USNA microfabrication laboratory. The following procedure was used to fabricate all the antennas and circuit boards described in this paper.

The starting material for the circuit boards was a square plate of substrate that was pre-coated on both sides, via electroplating, with 35.56 μm of copper. First, the plate was cleaned using sequential acetone, methanol, and isopropanol rinses. Then, photoresist was spin-coated onto the back surface of the plate, which was then baked at 100 °C for 2 minutes. This process was repeated on the front side of the plate. Photoresist is a liquid chemical resistant to metal etchants except when exposed to light. Spin-coating applies an even layer of photoresist across the plate

surfaces. A photograph of the spin-coater and hot plate used for circuit board fabrication is shown as Figure 17.

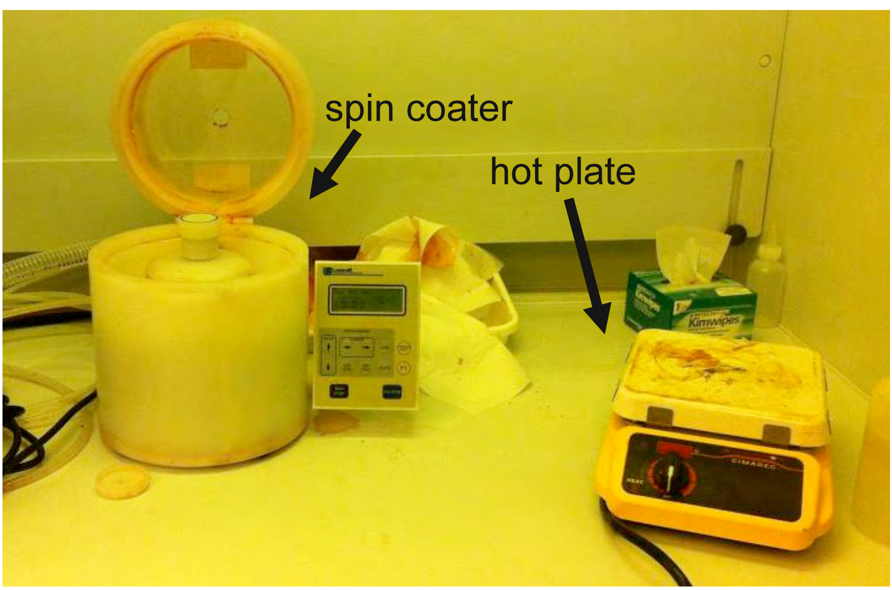

Figure 17: Spin-coater and hot plate used for circuit board fabrication

The spin-coated plate was then exposed to high intensity ultraviolet radiation under a chrome-on-glass mask that contained the layout of the antenna network as shown in Figures 14 and 15. By exposing the plates under the chrome-on-glass masks, the photoresist was only weakened in areas exposed to ultraviolet radiation, leaving a strong photoresist layer on top of desired metal traces and structures. Plates were generally exposed for about 12 seconds. A photograph of the ultraviolet exposure device is shown below as Figure 18.

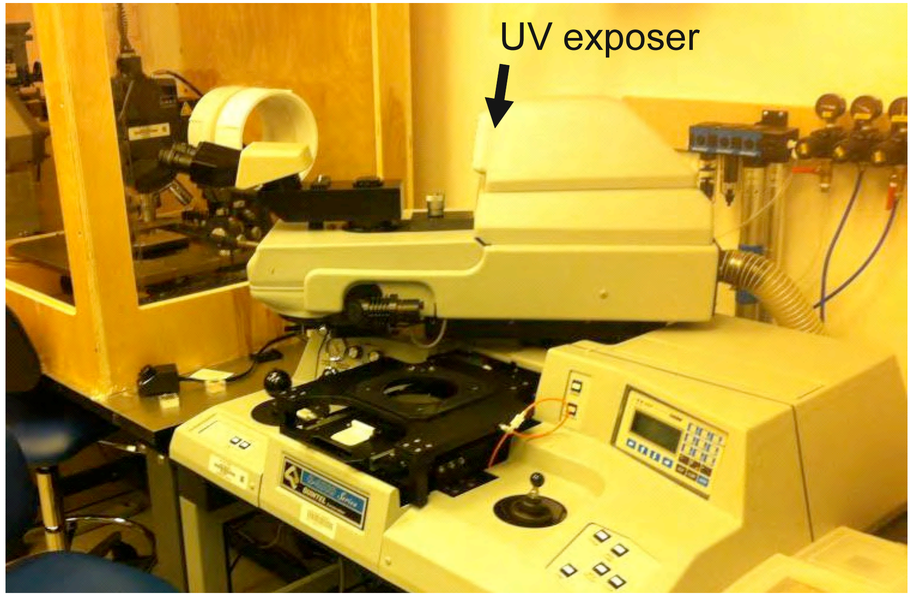

Figure 18: UV radiation exposure device used in circuit board fabrication

After exposure, the plate was placed in liquid AZ 300 MIF developer for about 10 minutes. The developer slowly removed the weakened photoresist from the plate, leaving only the photoresist protected from radiation by the chrome-on-glass mask. After development was complete, the plate was gently rinsed with distilled water, blow-dried, and baked for 2 minutes at 125°C.

The patterned plate was then immersed in ferric chloride (FeCl), a copper etchant that was heated to 60°–70° C. The etchant removed the copper that was not protected by the photoresist layers. This process took from 20 to 30 minutes. After etching was complete, the substrate was again washed in distilled water.

The remaining photoresist was removed from the plate with a solvent clean using sequential acetone, methanol, and isopropanol rinses. After then rinsing with water and blow drying, the circuit fabrication process was complete, and edge-mounted, 50 Ω SMA connectors were soldered onto the antenna circuit boards.

The surface mount components for the loaded microstrip antennas were soldered onto the landing pads by technicians at the Johns Hopkins Applied Physics Lab. The inductors were 0302-size wire-wound ceramic chip inductors designed by Coilcraft®, and the capacitors were 0402-size ceramic chips designed by Analog Technologies. Photographs of the fabricated baseline antenna and a loaded microstrip antenna are shown below as Figures 19 and 20, respectively.

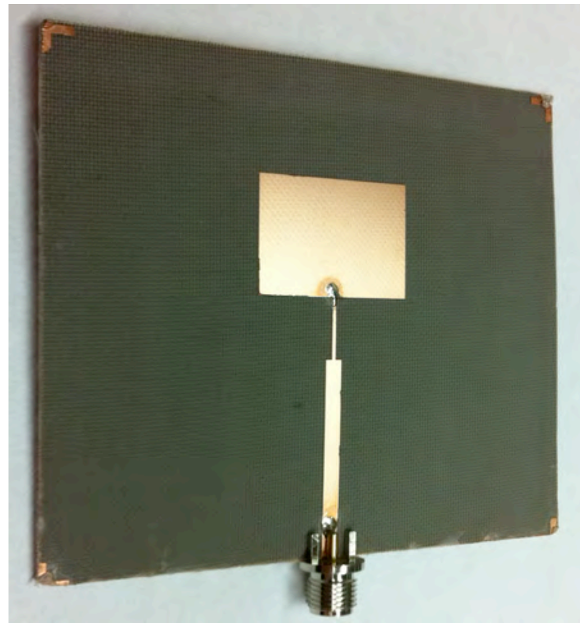

Figure 19: Baseline 5.5 GHz patch antenna

Figure 20: 5.5 GHz patch antenna with discrete reactive load

Microstrip Antenna Testing

Both the baseline and loaded patch antennas were tested using an Agilent E5071A vector network analyzer (VNA) and an anechoic chamber. A VNA is an instrument that measures network parameters such as return loss and gain for electrical circuits. An anechoic chamber is a room designed to prevent reflection of electromagnetic waves with radiation absorbent materials and unique geometries. Ideally, the chamber simulates an infinitely large volume of free space. Such a facility is necessary to characterize the radiation pattern of antennas. A photograph of the Naval Academy anechoic chamber is shown as Figure 21.

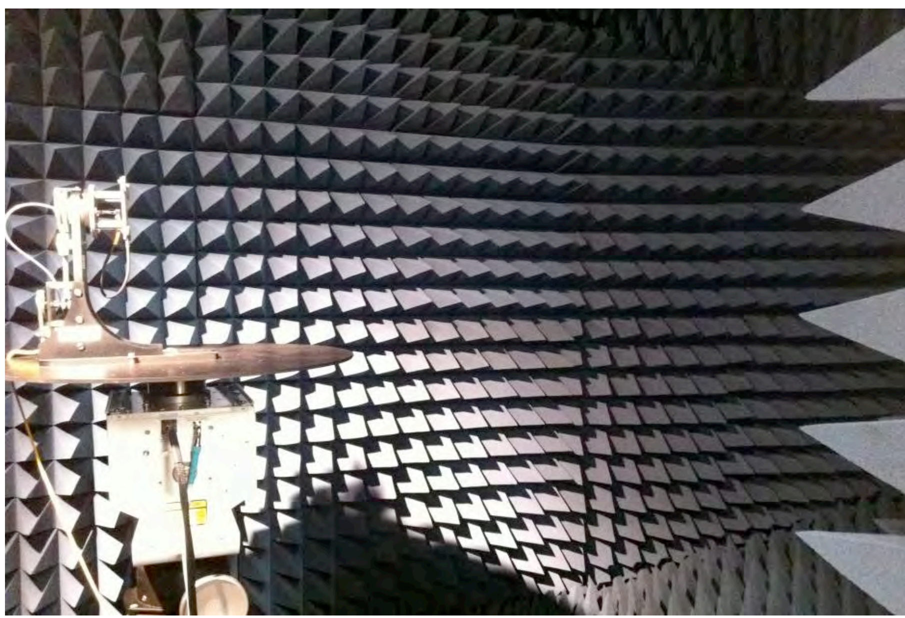

Figure 21: Naval Academy anechoic chamber

To test the return loss or S11 of the patch antennas, they were first attached to a single port of the VNA via the SMA connectors. The measured return losses of the unloaded and loaded antennas are shown below in Figure 22. An S11 minimum was observed at 7.27 GHz when the antenna was loaded with a 6.5 nH inductor and at 5.50 GHz when loaded with a 6.8 pF capacitor. Except when loaded with the 6.5 nH inductor, the antenna return loss characteristics matched simulated results within 5 dB and demonstrated similar qualitative behavior.

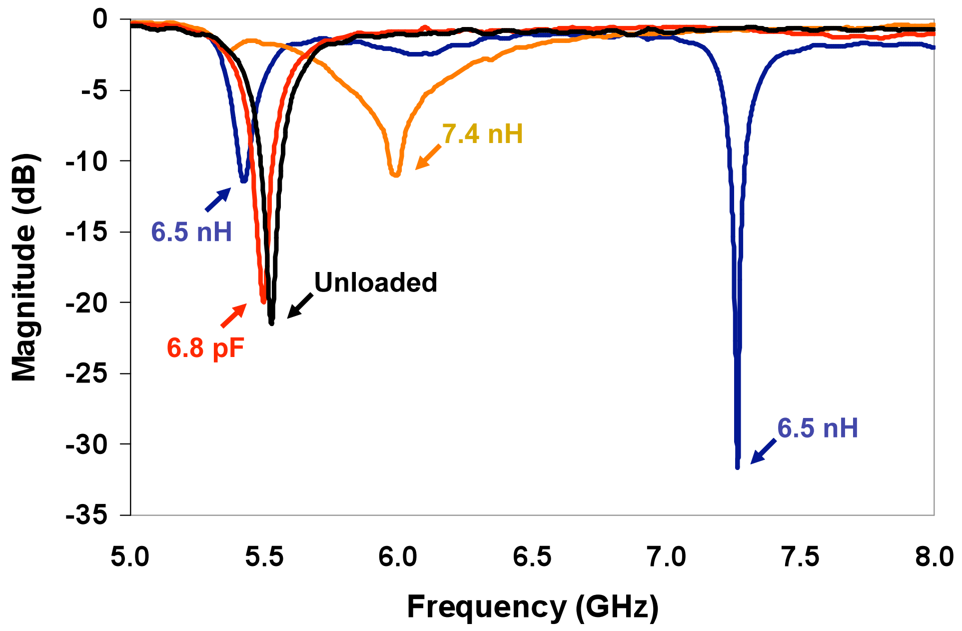

Figure 22: Measured return loss of loaded and unloaded 5.5 GHz patch antennas

When loaded with a 6.5 nH inductor, the minimum S11 differed in frequency from the expected 6 GHz operating frequency by as much as 1.27 GHz. Also, the simulated weaker resonance with a return loss of -3 dB at 5.35 GHz in the 6.5 nH loaded antenna was reflected in the measurement of a more pronounced resonant frequency at 5.4 GHz with a return loss of -11.4 dB. The difference between simulated and measured return loss characteristics may be a result of oversimplified models of the surface mount inductors and capacitors. The ideal inductances and capacitances used to model the loading components contain resistances and parasitic reactances that can cause a deviation of measured results from the simulation. Refer to Figures 16 and 22 for a graphical comparison between simulated and measured return loss characteristics for the proof of concept loaded microstrip antennas.

The loaded and unloaded microstrip antennas were also tested in an anechoic chamber, and radiation patterns were taken by connecting the VNA to a rotating antenna mount within the chamber. Azimuth radiation pattern data was recorded by setting up a high gain horn antenna at one end of the anechoic chamber as the transmission terminal Port 1 of the VNA. The patch antenna under test was connected to the VNA as the receiving terminal Port 2 of the VNA. The patch antenna was rotated in the azimuth plane by degrees, and the VNA records the power transmitted through the horn antenna and the power received by the patch antenna to determine antenna gain from a particular angle. A complete azimuth radiation pattern was recorded by

rotating the patch antenna under test by 360°. A diagram of the anechoic chamber test setup is shown below as Figure 23.

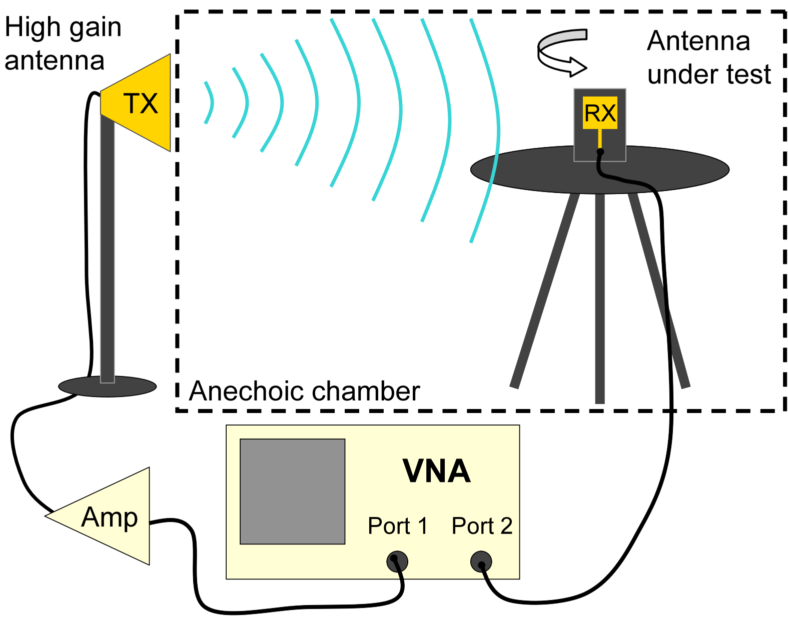

Figure 23: Diagram of radiation pattern test setup

The azimuth-oriented radiation patterns for the unloaded, 6.5 nH loaded, 7.4 nH loaded, and 6.8 pF loaded antennas at their frequencies of greatest gain are shown in Figures 24, 25, 26, and 27, respectively.

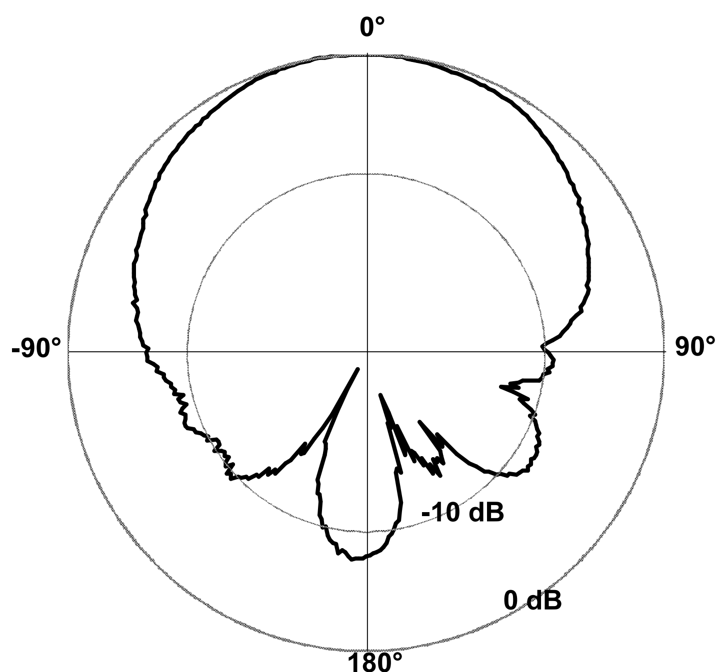

Figure 24: Radiation pattern of unloaded patch antenna at 5.54 GHz

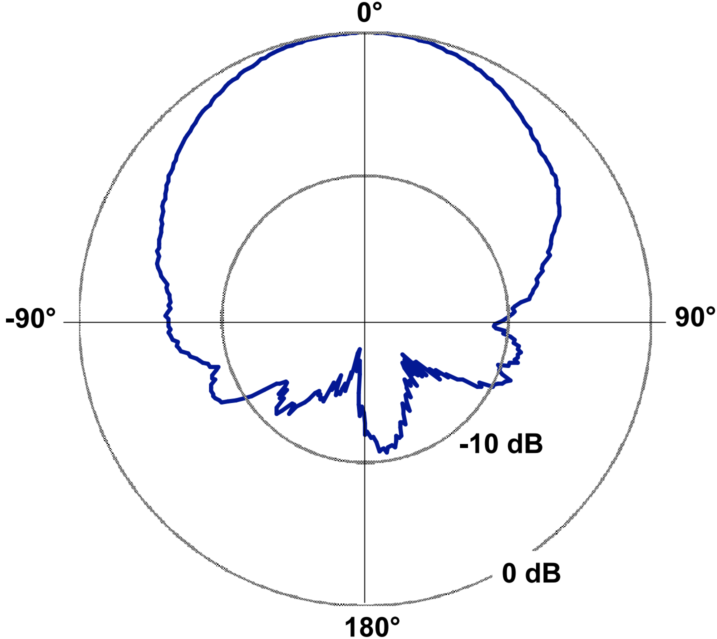

Figure 25: Radiation pattern of 6.5 nH loaded patch antenna at 6.36 GHz

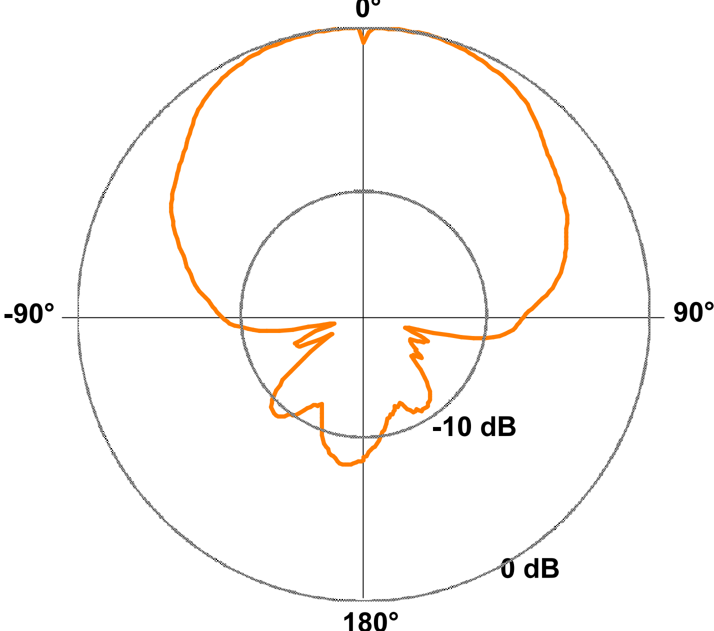

Figure 26: Radiation pattern of 7.4 nH loaded patch antenna at 5.99 GHz

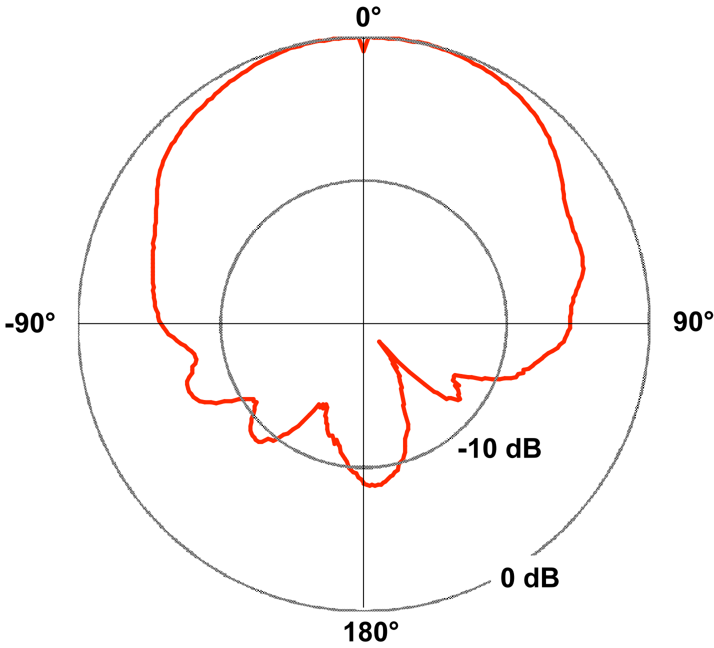

Figure 27: Radiation pattern of 6.8 pF loaded patch antenna at 5.47 GHz

Microstrip Antenna Data Analysis

The radiation pattern results of the tested microstrip antennas closely align with the simulated S11 results, but there is a discrepancy between the measured and simulated S11 results. From the data taken during the radiation pattern test, the unloaded antenna was found to resonate best at 5.54 GHz, which agreed with simulated and measured return loss data. The 7.4 nH and 6.8 pF loaded antennas resonated at 5.99 GHz and 5.49 GHz, respectively, as predicted. The 6.5-nH antenna maintained a largely resonant antenna pattern in the 5.5 to 7.25 GHz range, achieving its best performance at 5.53 GHz and 6.3 GHz. At their respective resonant frequencies, all the antenna radiation patterns matched the general expected behavior for rectangular patch antennas.

The better alignment between simulated return loss results and radiation pattern measurements is particularly noticeable in the 6.5 nH loaded antenna, whose 6.36 GHz measured resonant frequency represents only a 6% difference from the simulated resonant frequency. The measured S11 characteristic for the same antenna suggests a resonant frequency of 7.27 GHz, which represents a 21% difference between simulation and measurement. This suggests that the measured S11 characteristic of the 6.5 nH loaded antenna may be compromised.

Yet overall, the measured antenna results support the concept of antenna tuning using inductive and capacitive loads. Using discrete surface mount inductors and capacitors between 6.8 pF and 7.4 nH, a operating frequency shift between 5.47 GHz and 6.36 GHz was achieved. Having demonstrated changes in operating frequency using different discrete reactive loads, it follows that variable reactive components can be used to tune patch antenna operating frequencies.

Microelectromechanical Systems

Microelectromechanical systems (MEMS) are used in reconfigurable antenna design because of their ability to serve as switches, phase shifters, and tunable reactive elements with low power consumption, low insertion loss, and high linearity [3]. The objective of this research is to develop MEMS variable inductors and capacitors able to serve as variable reactive loads for antenna tuning applications.

Due to time and cost constraints, a multi-user MEMS process was preferred for microchip manufacture. In a multi-user fabrication process, a foundry performs a predefined sequence of microfabrication steps, using mask sets that are provided by individual users. This allows for individuals to take advantage of the economy of scale that characterizes silicon chip manufacture. Layer materials and thicknesses are therefore the same for all users, but the layout is completely customizable. After comparing different multi-user processes, MetalMUMPs, illustrated in Figure 28, was selected as most suitable to this application. MetalMUMPs is a surface micromachining process with polysilicon, silicon nitride, nickel, and gold structural layers, and sacrificial oxide layers. The process also incorporates a bulk etching step for selective removal of portions of the silicon substrate [16].

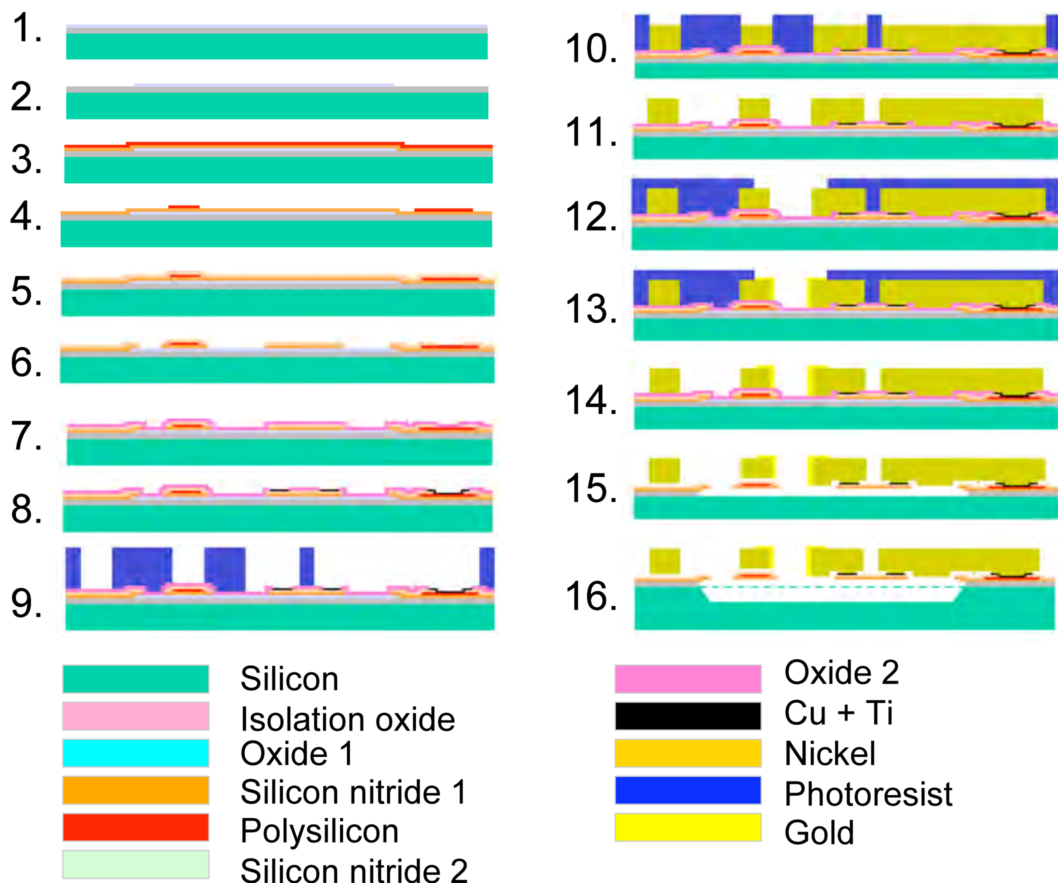

Figure 28: MetalMUMPs process summary [16]

This process was chosen over the other available options because of the thick electroplated nickel layer which could be used to create an acceptably low-loss transmission line. MEMS design is fundamentally tied to the fabrication process. While there would be more design flexibility with a completely custom process, a multi-layer custom process can take years to develop. Working within the MetalMUMPs design space constrained the design but allowed for a relatively fast fabrication turn-around and greater device yields.

MEMS Variable Capacitor Design

The MEMS capacitors reported here were an original design that features nickel and polysilicon layers as the movable plates of a variable parallel plate capacitor. The polysilicon layer was embedded in silicon nitride for electrical isolation and suspended over a trench in the silicon substrate. The nickel capacitor plate was suspended over and perpendicular to the polysilicon layer. This nickel bridge also served as the RF signal line for the capacitor. A diagram of the capacitor is shown below as Figure 29.

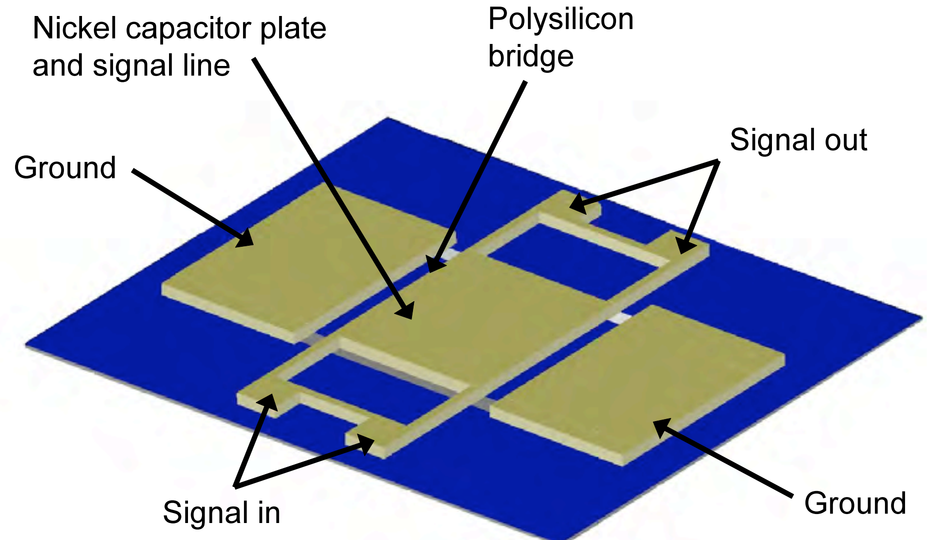

Figure 29: Diagram of MEMS capacitor, isometric view

To achieve electrostatic actuation, the polysilicon-silicon nitride membranes included embedded, isolated patches of polysilicon at each end of the membrane bridge. These patches lay beneath the suspended edge of grounded nickel structures that flanked each side of the nickel capacitor bridge as shown in Figure 30. When a DC voltage was applied to the embedded, isolated patches of polysilicon, an electrostatic force pulled the entire polysilicon-silicon nitride bridge up, decreasing the distance between the nickel capacitor bridge and the center polysilicon plate. This variable distance between the nickel bridge and the center polysilicon plate resulted in a change in capacitance seen by an RF signal passing through the nickel bridge.

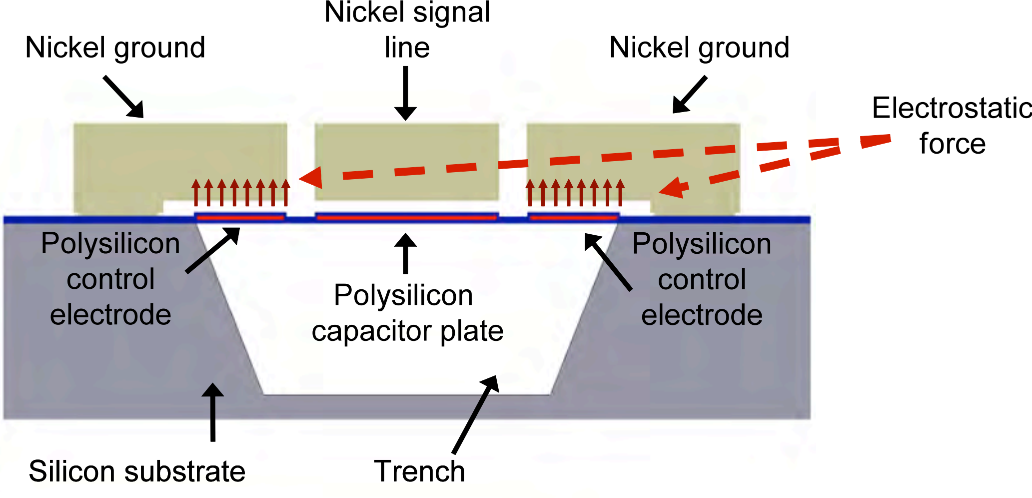

Figure 30: Diagram of MEMS capacitor, side view

The design choice for electrically isolated polysilicon electrodes in the underlying membrane was driven by the desire to separate the DC bias voltage from the signal line and also by the need for a conductive signal line material. Nickel was chosen as the signal line material, and the isolated control electrodes in the underlying membrane allowed variability without directly affecting any of the structures that comprise the capacitor except the distance between them.

The capacitance C of the described MEMS device was derived from the parallel plate capacitor model and is given by Equation 26 where ε_r is the relative dielectric constant between the nickel signal line and the embedded center polysilicon plane, g is distance between the signal line and polysilicon plane, and t_d is the thickness of the insulating silicon nitride layer between the polysilicon and the nickel. This design equation does not account for fringing capacitance, which will increase the overall capacitance of the component. A close up side view of the capacitor is shown below as Figure 31 [17].

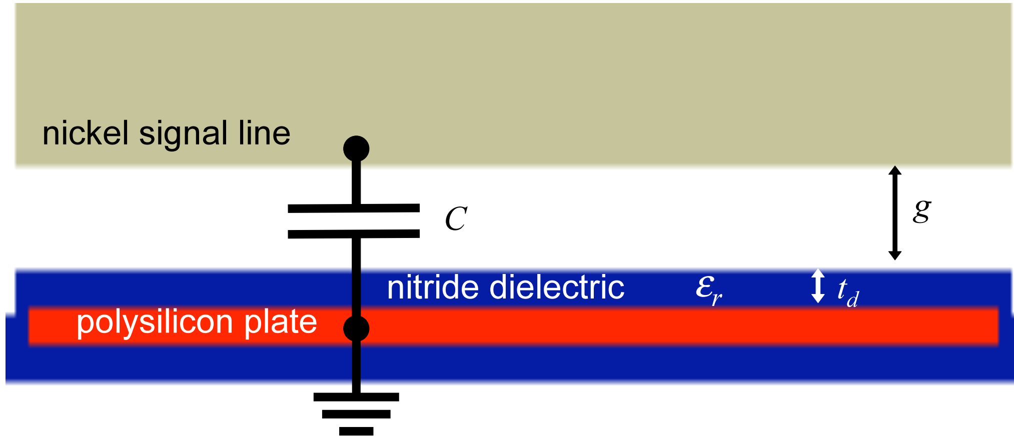

Figure 31: Diagram of MEMS capacitor, close up side view

$$C = \frac{\varepsilon_0 A}{g + \left(\frac{t_d}{\varepsilon_r}\right)} \tag{26}$$

The electrostatic force that pulled up the polysilicon-silicon nitride membrane was induced by applying a DC voltage to the flanking polysilicon plates and grounding the flanking nickel structures that overhang them. To hold the membrane up, the electrostatic force must exceed the mechanical restoring force, requiring a pull-in voltage V_{pi} given by Equation 27 [17] where ε_f accounts for capacitance losses due to roughness on the nickel and silicon nitride surfaces; g represents the distance between the plates, and g_0 is the non-actuated distance between the plates. A_a is the effective area of the overlapping nickel and polysilicon actuating structures.

$$V_{pi} = \sqrt{\frac{2k_e}{\varepsilon_f \varepsilon_0 A_a}(g_0 - g)\left(g + \left(\frac{t_d}{\varepsilon_r}\right)\right)^2} \tag{27}$$

The expression for the mechanical restoring force, F_m, is given by Equation 28 [17]where k is the partial spring constant of a fixed-fixed beam, which is given by Equation 29 [17] where E is Young's modulus of the polysilicon membrane, w is the width of the membrane, l is the length, and t is the thickness of the membrane. The quantity x is the length from the end of the bridge to the closest point where electrostatic force due to the far electrode affects the beam as shown in Figure 32. The biaxial residual stress is represented by σ, and v is Poisson's ratio. The constant for the non-linear term in the restoring force k_s is given below as Equation 30 [17].

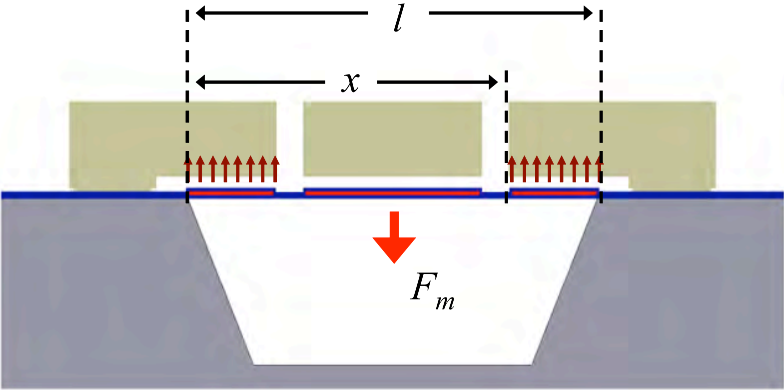

Figure 32: Diagram of MEMS capacitor showing mechanical restoring force

$$F_m = k(g_0 - g) + k_s (g_0 - g)^3 \tag{28}$$

$$k = 4Ew\left(\frac{t}{l}\right)\frac{1}{(x/l)(1-(x/l))^2} + 4\sigma(1-v)w\left(\frac{t}{l}\right)\frac{1}{1-(x/l)} \tag{29}$$

$$k_s = \frac{\pi^4 Ewt}{8l^3} \tag{30}$$

The equivalent Young's modulus, Poisson's ratio, and residual stress for the polysilicon-nitride membrane are the weighted volumetric average of the various layers. Thus, Young's modulus is given by Equation 31 [17] where E_n and t_n are the Young's modulus and thickness of each individual layer.

$$E_e = \frac{\Sigma E_n t_n}{\Sigma t_n} \tag{31}$$

The dimensions for the capacitors in this project were based on equations 26–31, all of which are documented in [17]. The targeted tunable capacitance range for the capacitors was between 0.75 pF to 1.5 pF for actuation voltages up to 6 V, which should be well below the pull-in voltage of the structure. While a wider capacitance range would be possible by considering flattening effects after pull-in, this operation has the disadvantage of non-continuous tuning and the possibility of the polysilicon-silicon nitride bridge acting as a capacitive switch, blocking RF transmission across the nickel signal line.

MEMS Variable Inductor Design

The MEMS inductors reported here were based on a design by I. Zine-El-Abidine and M. Okoniewski [7] and feature a pair of suspended pre-deformed coplanar nickel beams that buckle away from each other with the application of a lateral force via thermal actuation, resulting in a variable mutual inductance. The beams were electrically connected at the end closest to the actuating mechanism as shown in Figure 33, and the signal travels through each beam.

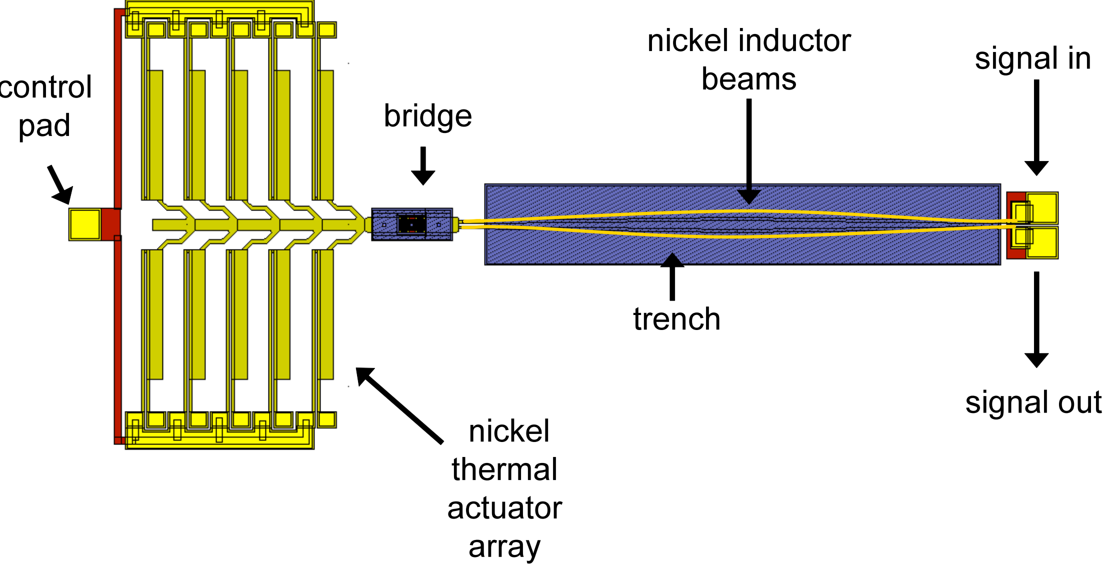

Figure 33: Diagram of MEMS inductor, top view

The cross-section dimensions (8 μm wide and 20 μm thick) and outward pre-deformation of the nickel beams predispose them to bend horizontally outwards instead of inwards or vertically when a lateral force is applied to the ends of the beams. The variable inductor design was modeled using COMSOL®, a multi-physics finite element modeling program. The resulting simulations of the inductor beams with 0 and 25 mN of lateral force are shown below in Figures 34 and 35, respectively.

Figure 34: Simulation of inductor beams under 0 N lateral force

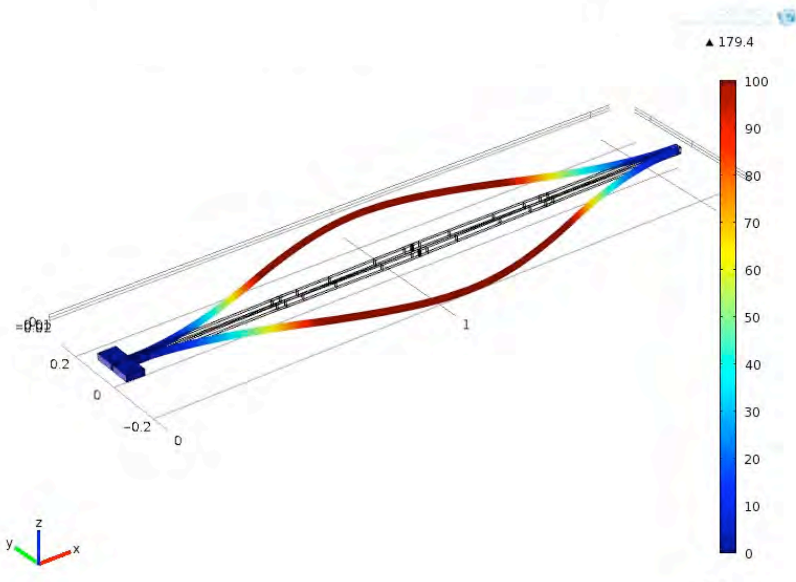

Figure 35: Simulation of inductor beams under 25 mN lateral force

An array of differential thermal actuators provided a lateral force when a voltage difference was applied across the actuators. The voltage difference induced a current that heated up the arms of

the actuator array, which consisted of a thin and thick component. A COMSOL® simulation of thermal actuator displacement at 100 V input and no load is shown below in Figure 36.

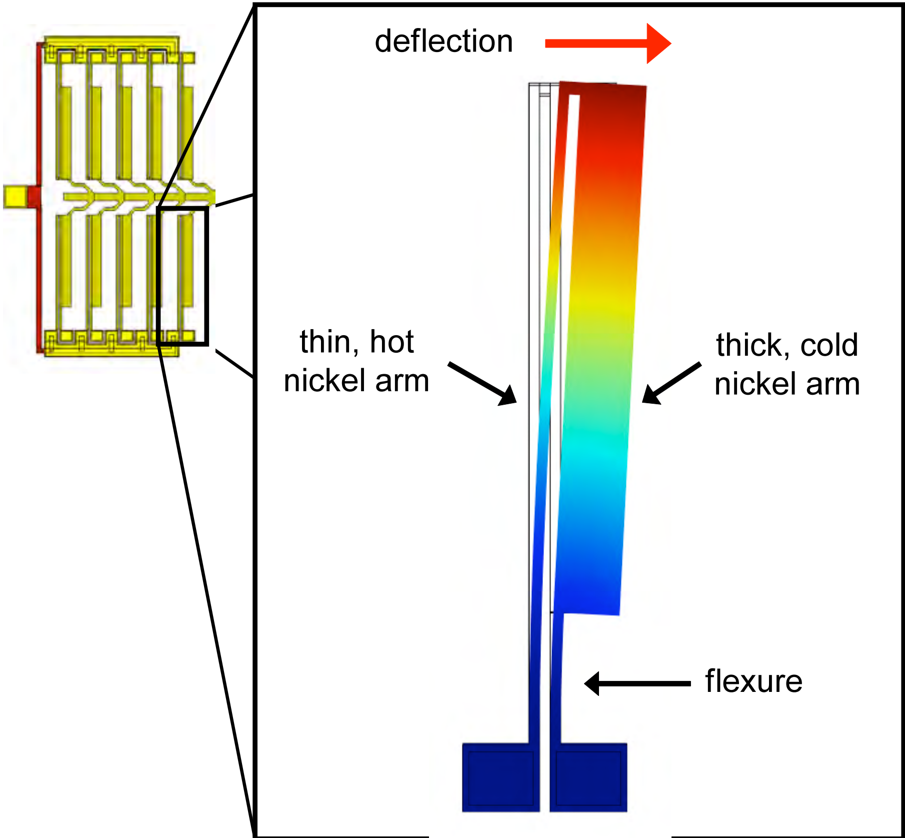

Figure 36: Diagram of thermal actuator

The temperature of the arms increased with current due to the resistance of the nickel structures. The resistance of an element R is proportional to material resistivity ρ and length l and inversely related to the element's cross sectional area A as described by Equation 32.

$$R = \frac{\rho l}{A} \tag{32}$$

Therefore, the thin arm represents a greater resistance than the thick arm and dissipates more power P as heat in accordance with Equation 33 where R is the resistance of the element and I is the current through the element.

$$P = I^2 R \tag{33}$$

The difference in dissipated power P as heat is reflected in an average difference in temperature between the two arms. This difference is translated into lateral motion by the phenomenon of thermal expansion. Because materials dimensions expand at higher temperatures, the thin, hot arm of the actuator structure expands more than the thick, cool arm. The difference in expansion results in a force that displaces the actuator structure laterally. When yoked together in an array

as shown in Figures 33 and 36, multiple thermal actuator arms can apply a net lateral force on the inductor beams.

The thermal actuator array is coupled to the inductor beams via a silicon nitride bridge suspended over a trench in the silicon substrate. A bridge structure is necessary in order to prevent the actuator structures from electrically coupling to the inductor beams. By affixing the end of the actuator yoke structure and the joined end of the inductor beams to a non-conducting silicon nitride bridge, simultaneous electrical isolation and mechanical connection is achieved. A diagram of the bridge structure is shown below in Figure 37.

Figure 37: Diagram of electrically isolated, mechanically coupled bridge, side view

MEMS Fabrication

The mask layout was drawn using MEMSPro, which incorporates L-EDIT layout software. The MEMS components were fabricated through the aforementioned multi-user nickel electroplated micromachining MetalMUMPs process [16]. The process allowed for only two conducting layers: a 21-μm thick electroplated nickel layer and a 0.7-μm thick polysilicon layer on an n-type silicon substrate. Two 0.35-μm thick silicon nitride layers can be used for structural support and electrical isolation between the polysilicon and nickel layers. Three sacrificial oxide layers allow for trench etching in the silicon substrate and physical separation of the conducting layers. Refer to Figure 28 on page 29 for a graphical summary of the of the 16-step MetalMUMPs process. For a detailed description, refer to the excerpt from the MetalMUMPs Design Handbook included as an appendix to this report.

Photographs of the featured MEMS capacitor and inductor are shown below in Figures 38 and 39, respectively.

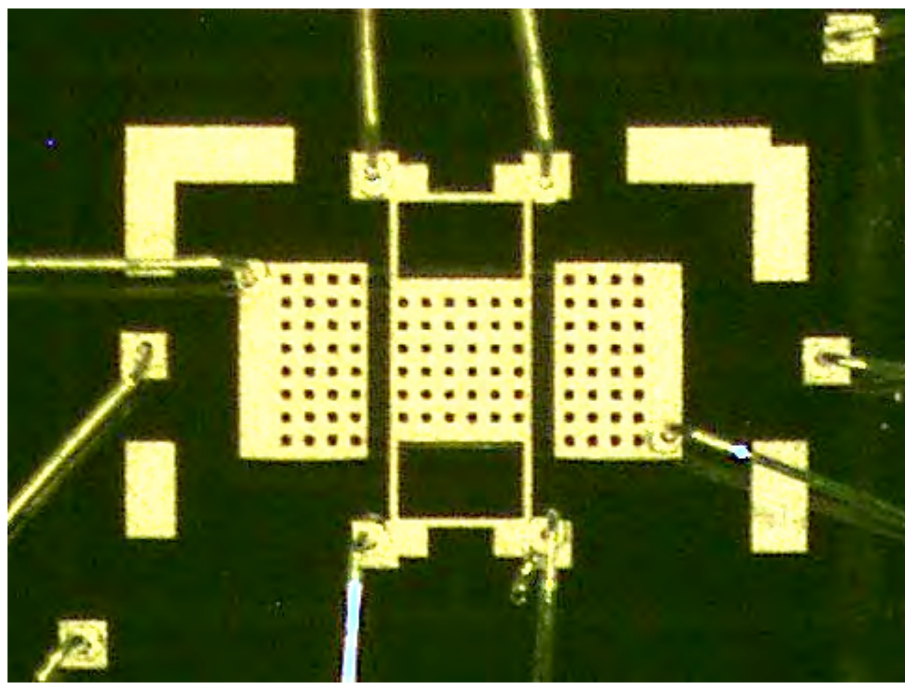

Figure 38: Photograph of MEMS variable capacitor

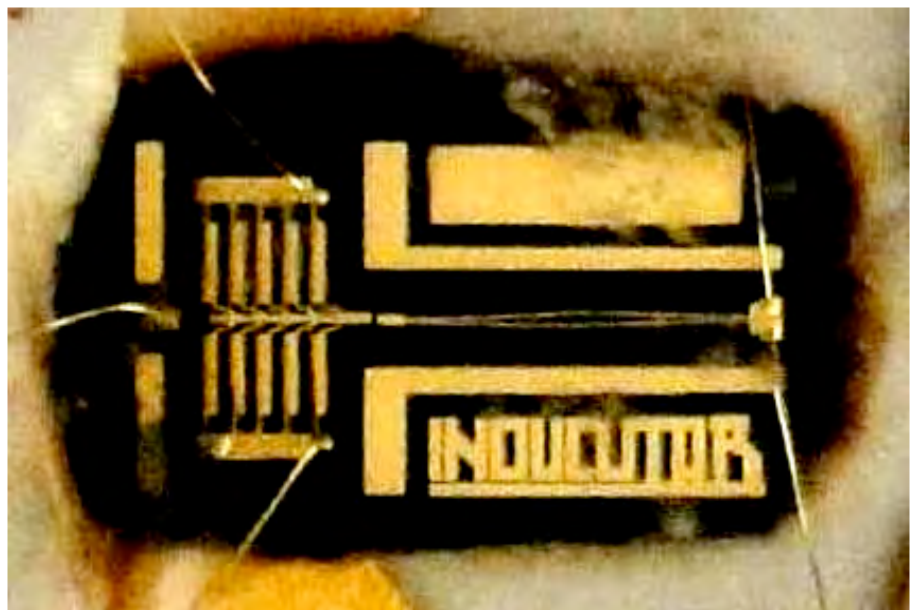

Figure 39: Photograph of MEMS variable inductor

The MEMS components were delivered as 15 one-square-centimeter sets further diced into nine dice as directed. The previously described MEMS capacitor and inductor have dimensions of 1.67 mm by 2 mm and 3.33 mm by 2 mm, respectively. To maximize the number of devices per run and minimize dicing costs, the capacitors were arranged two devices to a die. The entire one-square-centimeter sets include other devices designed by the author, including alternative capacitors, switches, and matching networks that are not discussed in detail here due to limited testing. The entire mask set is included as an appendix to this report.

MEMS Device Testing

In order to test the MEMS components, testing circuits consisting of a 50 Ω microstrip or coplanar waveguide transmission line and as many as 14 DC control lines were fabricated using the process described on pages 21–23. The circuits were then electroplated with a 1 μm gold layer, a negligible height difference, to allow a wire bonding to the MEMS devices. The testing circuits and MEMS elements were joined using EPO-TEK H67-MP non-conductive epoxy. The MEMS devices were then connected to the control lines by gold wire bonding, a technique that uses heat, pressure, and ultrasonic energy to affix a 1-mil diameter gold wire to two electrodes, one on the MEMS chip and the other on the control line accessible from the exterior of the O-ring and microscope slide fragment used to placed over the MEMS devices to protect them. Epoxy application and wire bonding were conducted at the Johns Hopkins Applied Physics Laboratory. Photographs of the previously discussed MEMS capacitor mounted and wire bonded on a microstrip test circuit are shown below as Figure 40.

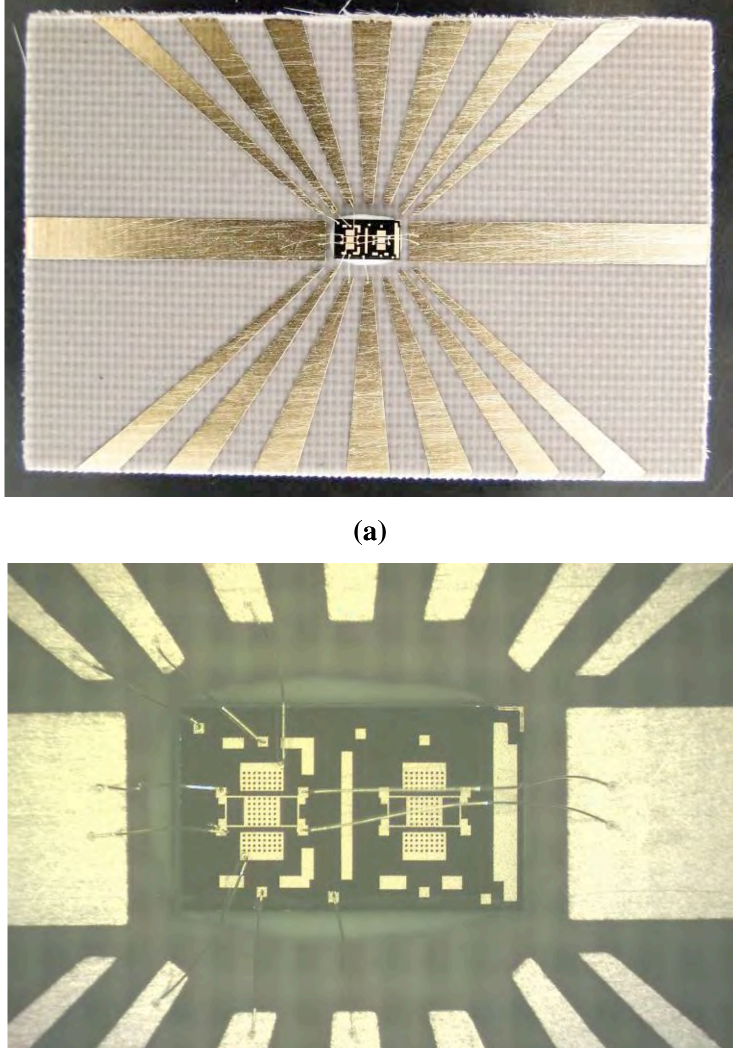

(a)

(b)

Figure 40: (a) MEMS variable capacitor mounted on test circuit (b) close up view

The MEMS devices were tested with varying DC control inputs using the Agilent E5071A VNA described previously. For the inductor devices, mechanical data was also simultaneously recorded using a Wyko optical interferometer. The test setup is shown below as Figure 41.

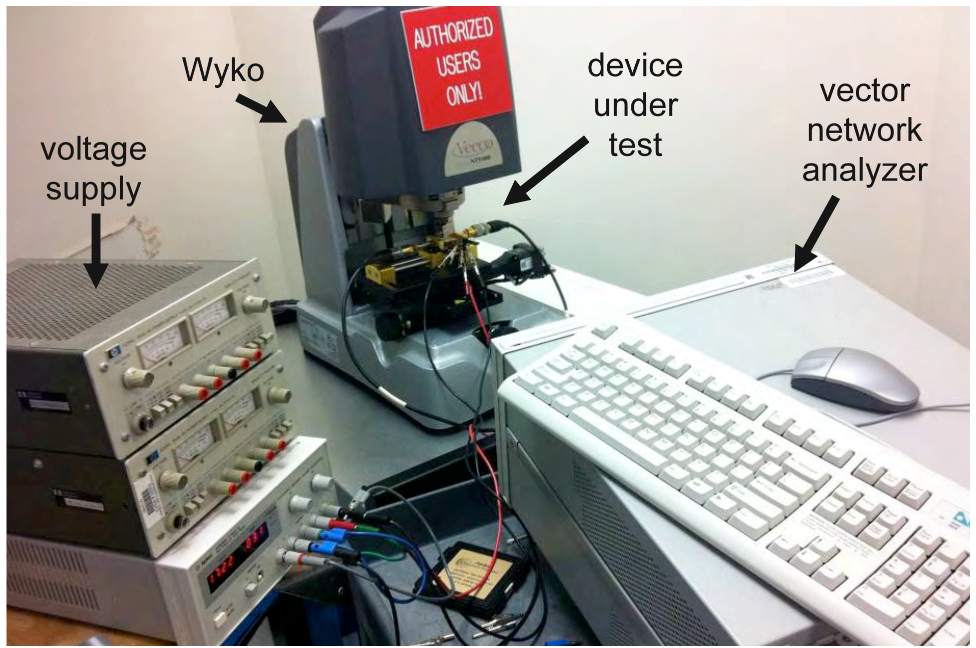

Figure 41: MEMS device test setup

The measured capacitance of the previously described MEMS variable capacitor for actuation voltages from 0–30 V is shown in Figure 42.

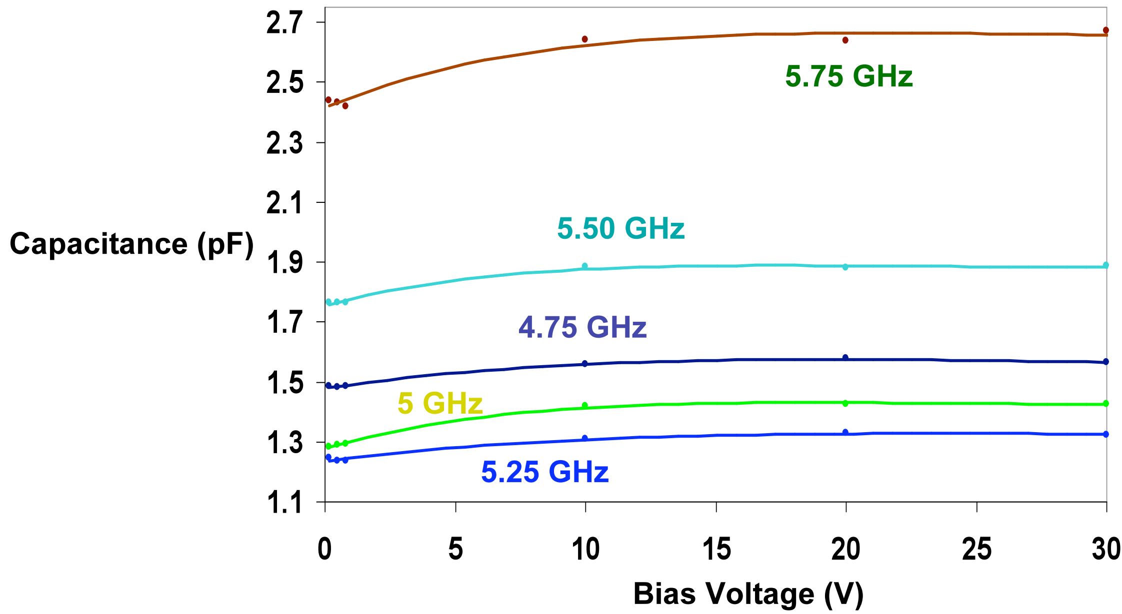

Figure 42: Measured capacitance of MEMS variable capacitor with trendlines

The capacitor demonstrated an increase in capacitance between 0.1 and 0.25 pF with increasing actuation voltage over the range of 0–20 V at frequencies greater than 4.75 GHz and less than 6 GHz. Beyond 20 V, the measured capacitance remained constant, indicating that the membrane and the overhanging nickel structure had made full contact.

The measured capacitance values in Figure 42 most likely exceed the designed capacitance range of 0.75–1.5 pF due to fringe capacitance. Fringing occurs due to the extension of the electric field beyond the area directly overlapped by capacitor plates. Fringing effects are significant in small geometries, where the increased effective capacitor area due to fringing represents a large fraction of the designed capacitor area. This results in fringe capacitances that are typically 15% to 40% as large as designed capacitance [17]. Fringe capacitances may be even larger in the MEMS capacitor devices reported here due to the proximity of the control electrodes to the signal line.

Another issue encountered during testing was the need to discharge the control electrodes after actuation. Under the current configuration, no internal safe discharge method exists. An external resistor was used to help discharge the structures during testing. Due to this limitation and limited time available for further testing, the capacitor design was not integrated into a patch antenna network.

Inductance measurements made using the VNA for the featured MEMS inductor are shown below in Figure 43 under no actuation and an actuating voltage of 100 V. A clear decrease in inductance is noted for increasing actuation voltage. An inductance range from 1.16 to 0.94 nH at 5 GHz for input voltages between 0 and 100 V was demonstrated successfully. This inductance range closely matched the intended design goals although the required actuation voltages to achieve this inductance range exceeded the expectations.

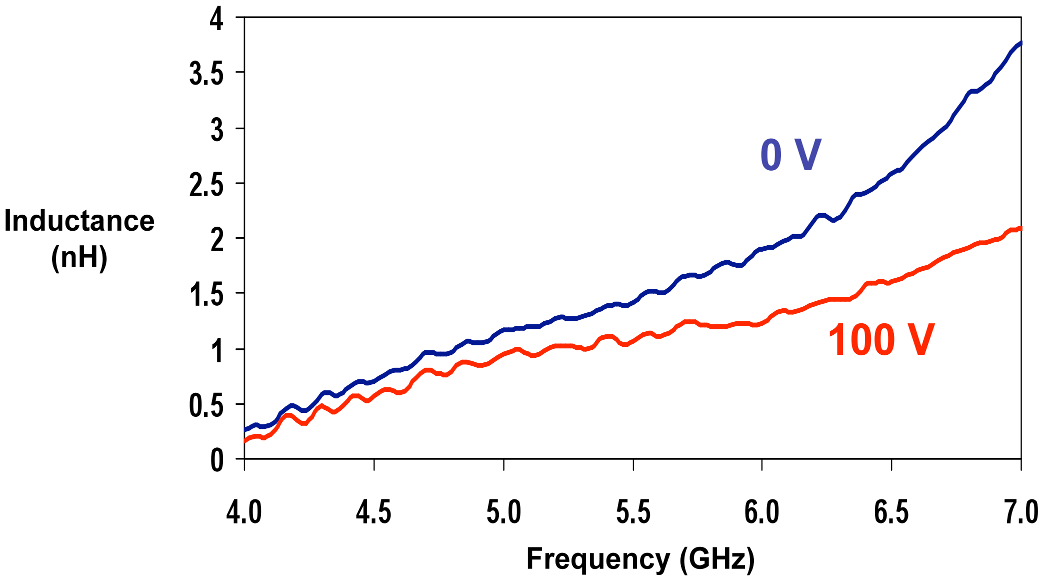

Figure 43: Measured inductance of MEMS variable inductor

Damage to the bridge structure coupling the inductor and actuator mechanically during fabrication is the most probable source of the high actuation voltage levels required. A Wyko

rendering of the bridge structure under no input voltage and at 25 V input voltage is shown in Figure 44 below.

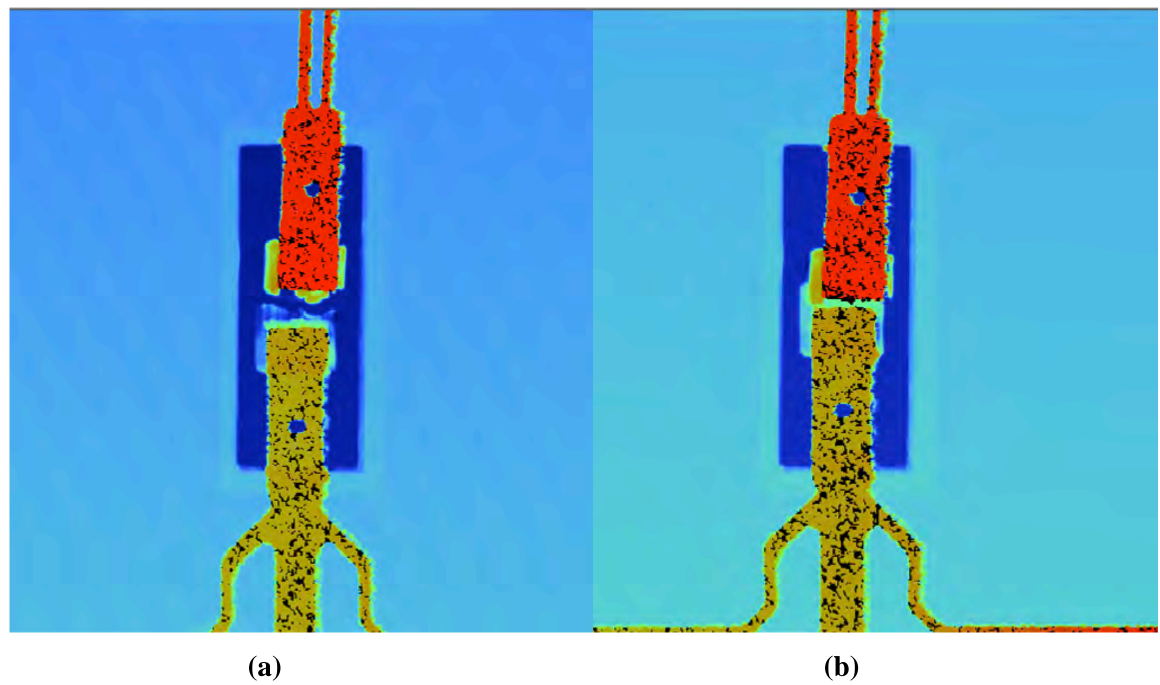

(a) (b)

Figure 44: (a) Wyko rendering of bridge structure at 0 V and (b) at a 50 V bias voltage

The crack observed in Figure 44 was due to the stress applied to the bridge structure during the etching of the silicon trench beneath the bridge in the fabrication process. The crack breaks the direct mechanical connection between the actuator array and the inductor beams. However, the actuator can still apply lateral force on the free end of the actuator but at higher actuation voltages. As seen in Figure 44 (b), the gap formed by the crack in the bridge structure is closed at an input voltage of 50 V, allowing force to be applied to the inductor beams at higher voltage levels.

Another likely cause for higher than expected actuation voltages was damage to the inductor actuator array incurred during wire bonding. The ground pads of the inductor thermal actuator array proved to be too small for safe wire bonding, and some of the actuator arms were deformed upward during the process. A Wyko rendering of the MEMS thermal actuator array is shown below as Figure 45. Note that the upper right actuator is lifted at an angle to the substrate surface rather than parallel to it.

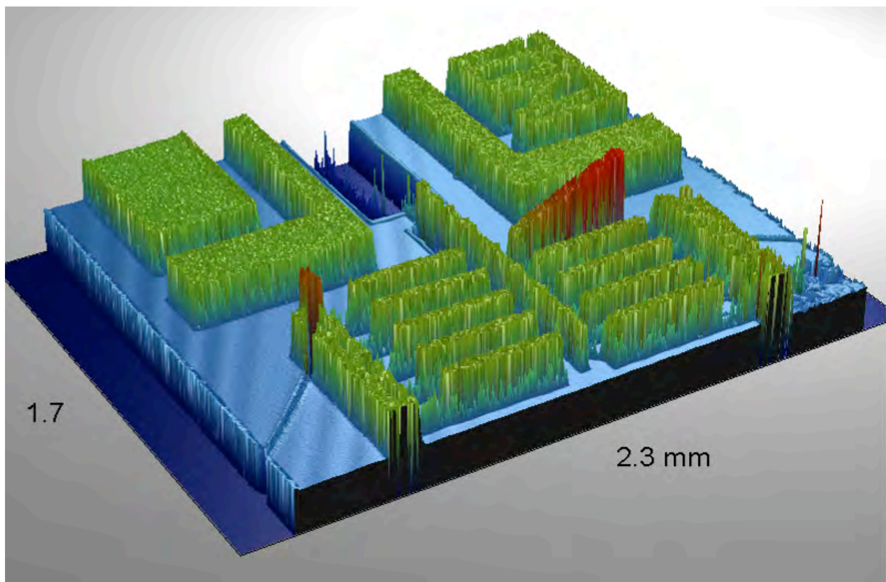

Figure 45: Wyko 3-D rendering of MEMS inductor actuator array

It is notable that while the inventors of this inductor design reported an increase in inductance upon actuation [7], this author has observed the opposite effect. Successful outward buckling of inductor beams as described by Zine-El-Abidine and Okoniewski was observed in the devices presented here using a Wyko interferometer, but the inductance measured using a VNA showed a clear decrease with increasing bias voltage.

Possible reasons for this discrepancy include the different methods used to measure device inductance. The measurements taken by Zine-El-Abidine and Okoniewski used 3 high-admittance, offset coplanar pads, two of which doubled as the anchors of the inductor beams [7]. The third pad was then de-embedded from the RF analysis. The inductors fabricated here featured only two signal pads for input and output, and no impedances were de-embedded. Another possible reason for the discrepancy between previously reported results [7] and those presented here include the effects of mounting and wiring the MEMS die onto a circuit board in the vicinity of microstrip and coplanar waveguide structures.

Although both the MEMS capacitor and the MEMS inductor designs achieved less than optimal performance, both nonetheless demonstrated the capability to vary reactance. In the future, improved bridge structures, ground pads, and bias pads may help achieve better inductor performance. The MEMS capacitors reported here can be improved by increasing the distance between the control electrodes and the capacitor structures, thereby reducing fringing effects. But given that the devices were first-run prototypes, even limited ability to vary capacitance or inductance represents an achievement and enables the MEMS components reported here to serve as proof of concept variable reactive loads for antenna tuning.

Integrated System

MEMS Coplanar Waveguide Antenna Design

In order to integrate the MEMS components designed for this research into a tunable patch antenna system, a CPW-fed rectangular patch antenna was designed. The decision to pursue a CPW-fed antenna design was motivated by the coplanar nature of the MEMS devices and the simplicity of an inset feed.

Using Equations 11 and 23–25, a 5 GHz rectangular patch antenna was designed for 762 μm thick Duroid® 6002 high frequency laminate with 1-oz. electrodeposited copper metallization layers. The material was chosen for its relatively low dielectric constant ε_r of 2.94 and availability. The software optimized antenna dimensions of the patch were 16.92 mm in length and 18.39 mm in width. Using Equation 21, the required inset feed distance Δx was calculated to be 5.87 mm. This dimension was then verified by Sonnet™ software simulation. To achieve an inset feed using a CPW transmission line, a via connecting the antenna and transmission line metallization layers through the dielectric substrate was required.

The 50 Ω CPW feedline was designed using Equations 13–19. A signal line width a of 1.52 mm and a gap width of 82.55 mm (b = 1.69 mm) were calculated and verified using Sonnet™ software simulation. The mask layouts for a baseline coplanar waveguide antenna without a MEMS variable reactive load are shown below as Figure 46.

Figure 46: Mask layouts for 5 GHz baseline CPW antenna, (left) feed, (right) antenna

In order to integrate a MEMS component into the CPW feedline for the loaded patch antenna, a 3.81 mm by 3.81 mm gap was designed in the feedline at a distance of 45.72 mm from the inset via. This distance was chosen to match the recorded antenna impedance of the baseline antenna using Equation 22. Control lines were designed for a separate board to minimize interference with the CPW transmission line. The mask layouts for the MEMS-integrated antenna including the control board are shown below as Figure 47.

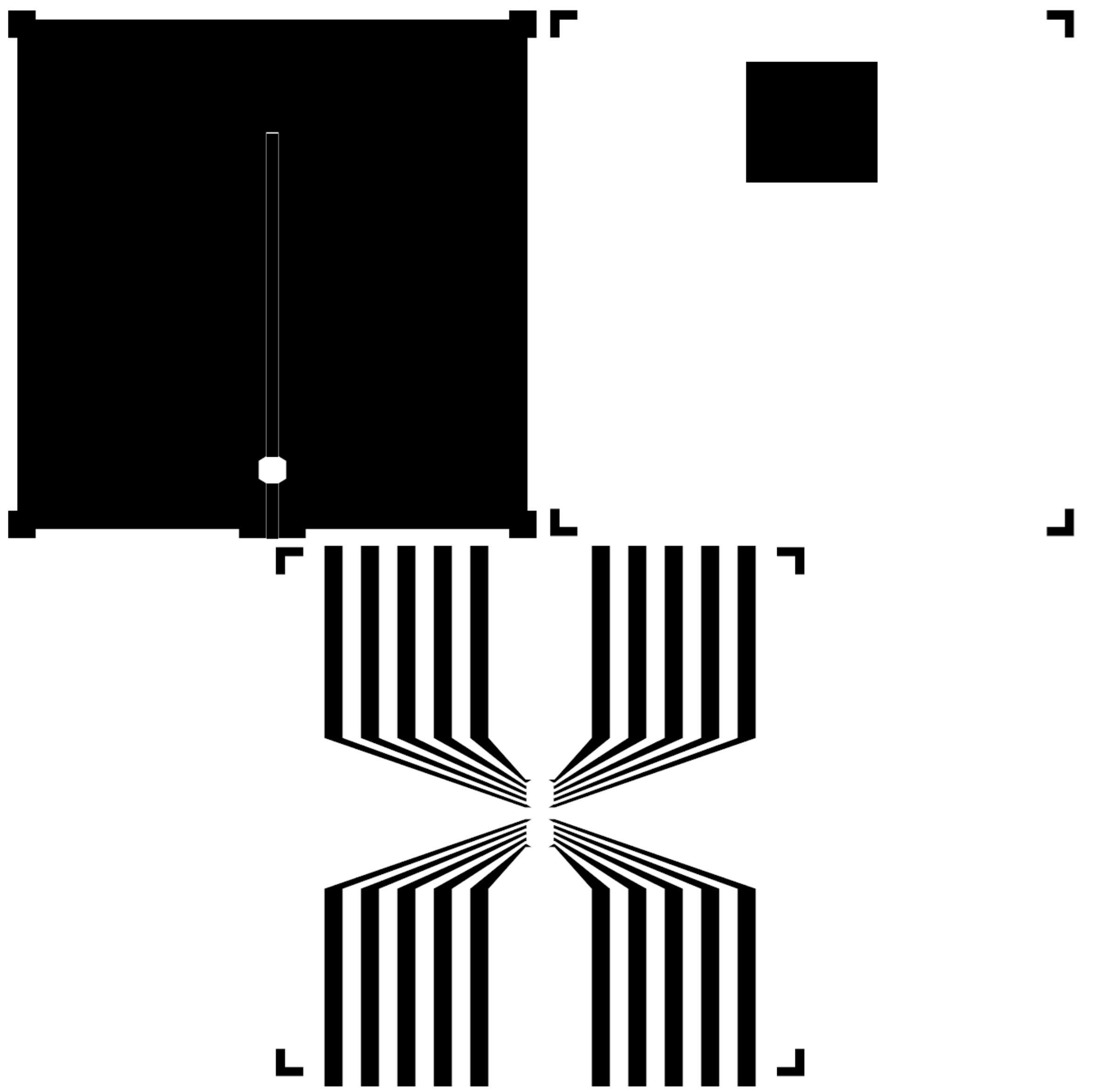

Figure 47: Mask layouts for MEMS-tuned antenna, (top left) feed, (top right) antenna, (bottom) control lines

Fabrication and Integration

Fabrication of the loaded and unloaded CPW-fed antenna designs followed the same procedures outlined on pages 21–23 used to etch the microstrip-fed antennas. However, wire bonding for the MEMS-loaded antenna required the metallization layers to be electroplated with a 1 μm thick gold layer.

After gold electroplating the substrates, including the control lines, the circuit boards were cut using shears and scissors and joined together using EPO-TEK H67-MP non-conductive epoxy. MEMS inductors were also joined to the antenna using the same epoxy. Next, the inductors were wire bonded to the control lines, SMA connectors were soldered onto the signal line traces, and a protective casing consisting of microscope slide glass and an O-ring was super-glued to the

board, covering the MEMS component. Again, epoxy application and wire bonding were conducted at the Johns Hopkins Applied Physics Laboratory. Finally, vias were drilled and soldered through the substrate at the desired inset feed location. An exploded view of the components of the MEMS-integrated antenna system is shown as Figure 48.

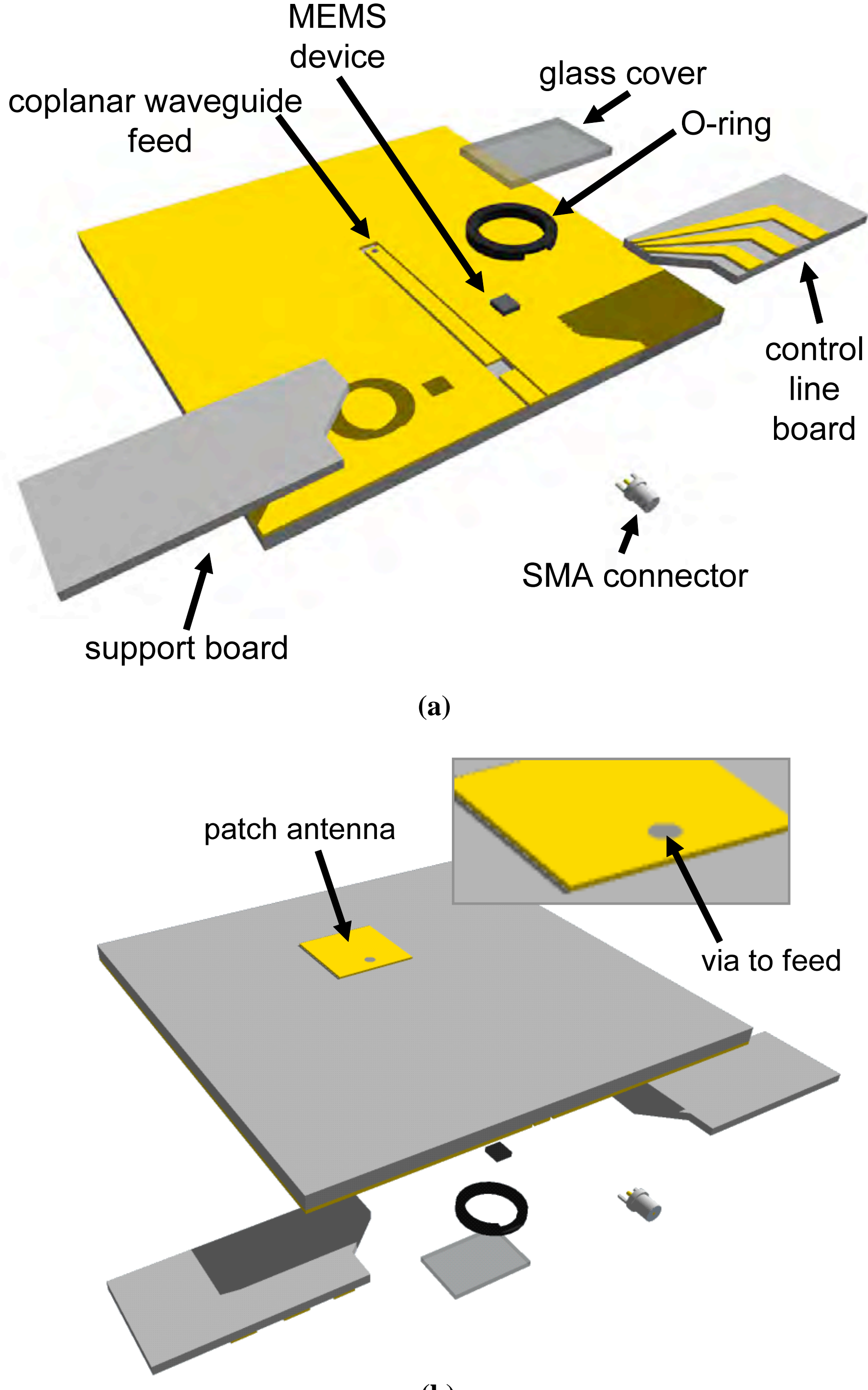

Figure 48: Diagram of (a) back and (b) front of MEMS-tuned antenna

Photographs of the complete MEMS-integrated antenna system are shown below as Figure 49.

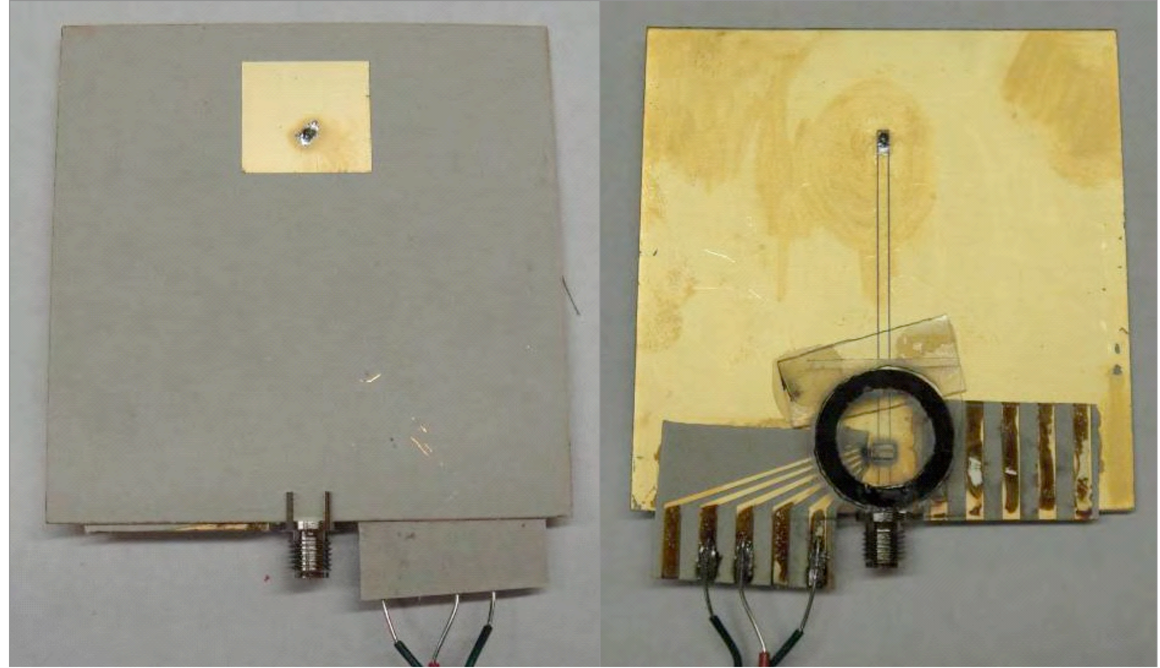

Figure 49: Photograph of front (left) and back (right) of fabricated MEMS-tuned antenna

Testing and Analysis

The baseline CPW-fed antenna return loss and the MEMS-loaded antenna return loss were tested using one port of the VNA while varying control voltages from 0 to 100 V. The measured return losses from 4.5–6.5 GHz are shown below in Figure 50.

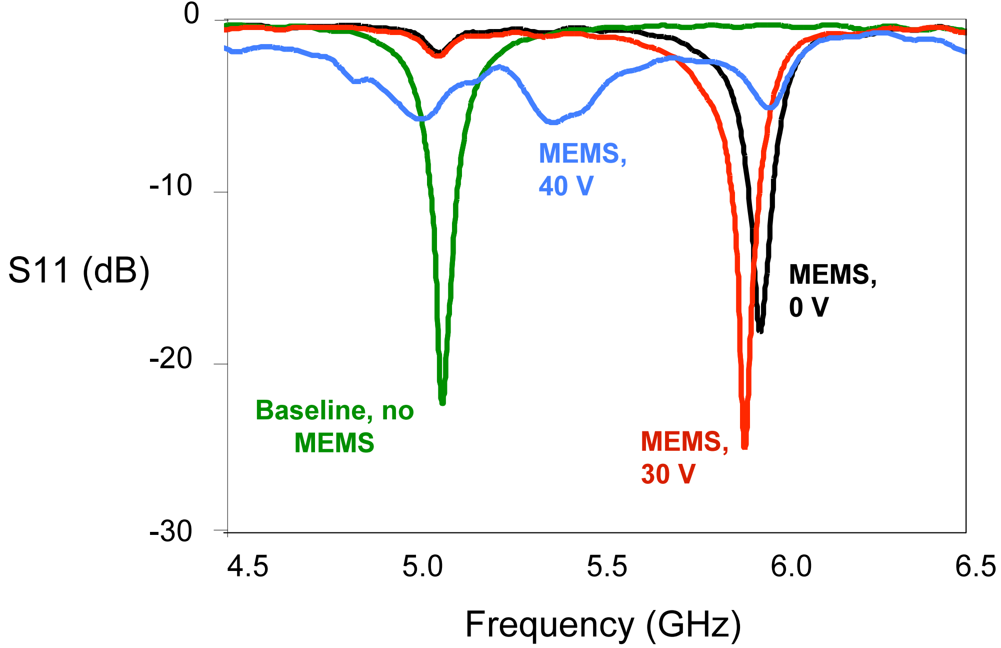

Figure 50: Measured return loss of CPW-fed antennas, 4.5-6.5 GHz

The return loss of the unloaded antenna indicated a minimum of -22 dB at an operating frequency of 5.08 GHz, which matched simulation and theoretical predictions. The MEMS-tuned antenna return loss showed a minimum of -18 dB at 5.94 GHz for an input control voltage of 0 V. At 30 V, the antenna return loss minimum shifted to -24 dB at 5.90 GHz. At higher voltages, return loss ceased to improve in the 4–6 GHz range. However, a higher, minor resonant mode around 7.9 GHz began to develop with increasing actuation voltage although return loss around that frequency never dropped below -10 dB for actuation voltages under 75 V. The return losses of the baseline and MEMS-tuned antenna from 7–8 GHz are shown below in Figure 51.

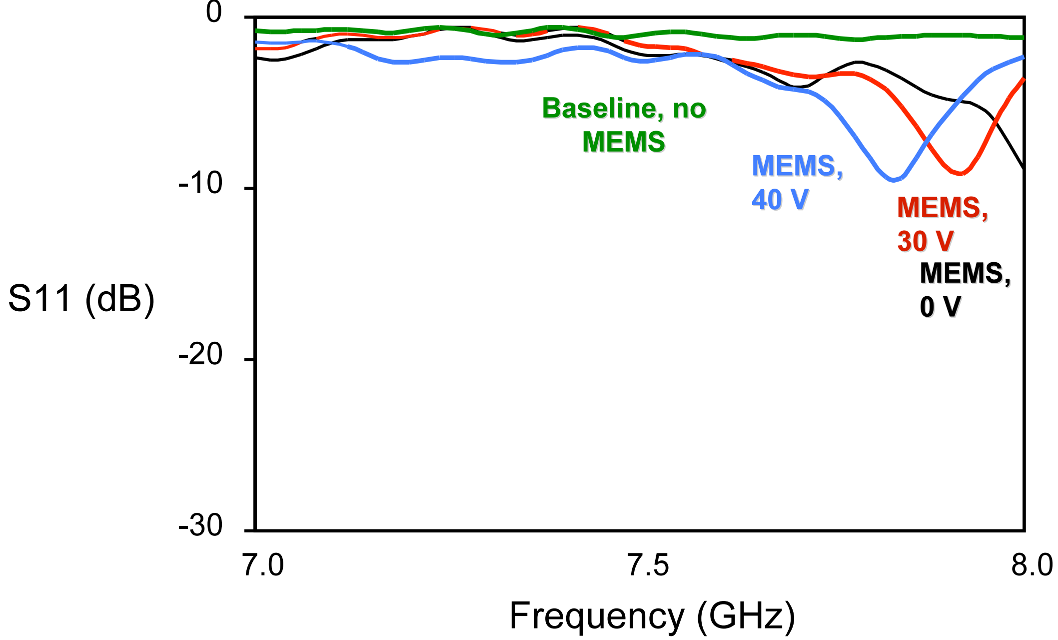

Figure 51: Measured return loss of CPW-fed antennas, 7-8 GHz

At 75 V the MEMS inductor burnt out, giving off a spark and breaking the bond wires to the control lines. The most likely reason for this failure was the high voltage used and the small distance between the DC control lines near the MEMS inductor. With high voltages and small distances, it is entirely possible that the dielectric strength of the environment near the MEMS inductor was overcome. The return loss of the MEMS-loaded antenna after the inductor burned out indicates two resonant modes at around 5.9 GHz and 7.9 GHz as shown below in Figure 52.

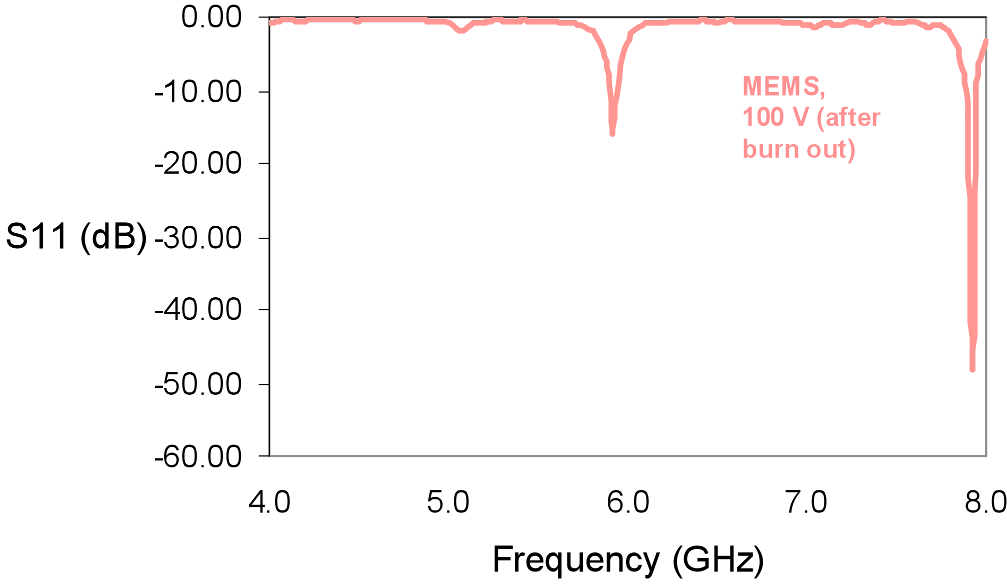

Figure 52: Measured return loss of MEMS-tuned antenna after device burn out

The shifts in the minimum return loss frequency of the MEMS-loaded antenna with varying input control voltage shown in Figures 50 and 51 indicate that the MEMS device successfully shifted the operating frequency of a patch antenna, a significant achievement. Even the return loss results after inductor burnout indicate that inductive loading can shift the resonant frequency of a patch antenna.

To verify the results of the return loss tests, the baseline CPW-fed antenna and the MEMS-loaded antennas with burned out devices were tested for radiation patterns in the anechoic chamber. The normalized results at 5.085 GHz, 5.895 GHz, and 7.85 GHz are shown below in Figure 53 for the baseline CPW-fed antenna and in Figure 54 for the MEMS-loaded antenna.

By comparing the radiation patterns of the two antennas across different frequencies, one observes that the MEMS-loaded antenna radiation patterns remain relatively coherent and directed normal to the plane of the antenna while the baseline antenna only radiates effectively in the 5 GHz mode. At 5.89 GHz, the baseline antenna's radiation pattern includes a strong null at -90° and significant back and side lobes. At the same frequency, the MEMS-loaded antenna maintains a strong main lobe in its radiation pattern with minimal increase in side lobe strength. At 7.85 GHz, the baseline radiation pattern almost takes on an end-fire radiation pattern but also includes strong nulls. At the same frequency, the MEMS-loaded antenna also includes nodes and some increase in side lobe strength but nonetheless maintains a main beam just 15° from the direction normal to the antenna. These results confirm that the MEMS-loaded antenna achieves relative resonance at frequencies other than the natural resonant frequency and therefore represents a MEMS-tuned antenna using variable inductors.

In summary, a MEMS variable inductor was integrated into the feedline of a rectangular 5 GHz patch antenna, achieving an upward frequency shift of 810 MHz from the antenna's natural resonant frequency, a 40 MHz continuous tuning range for bias voltages of 0–30 V, and a second resonant mode at 7.85 GHz.

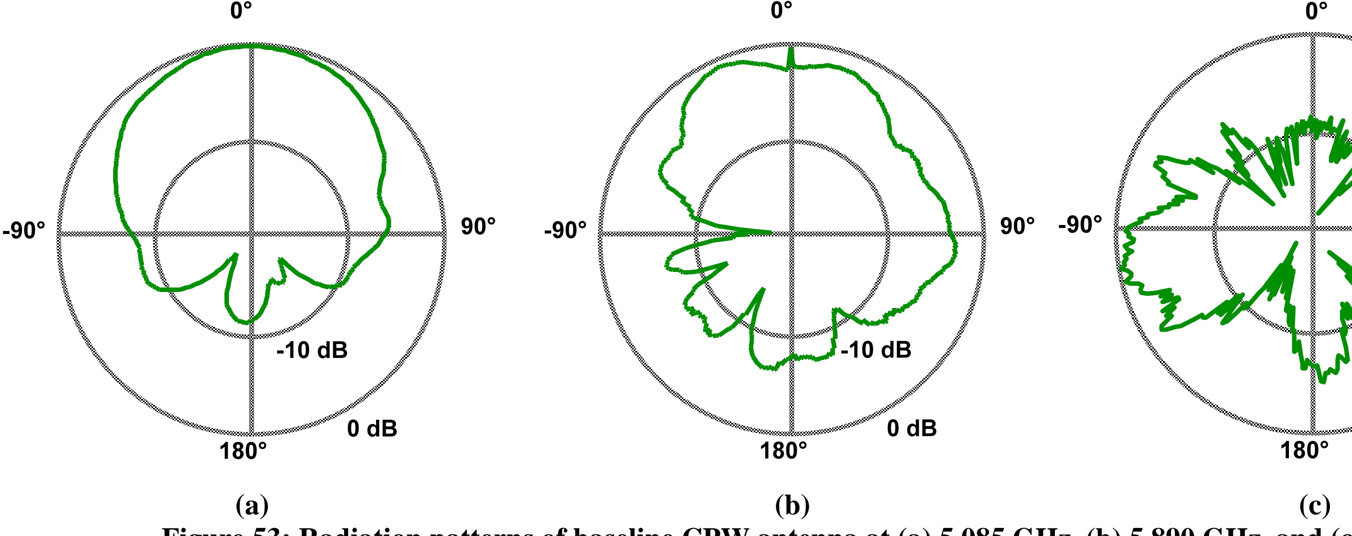

Figure 53: Radiation patterns of baseline CPW antenna at (a) 5.085 GHz, (b) 5.890 GHz, and (c

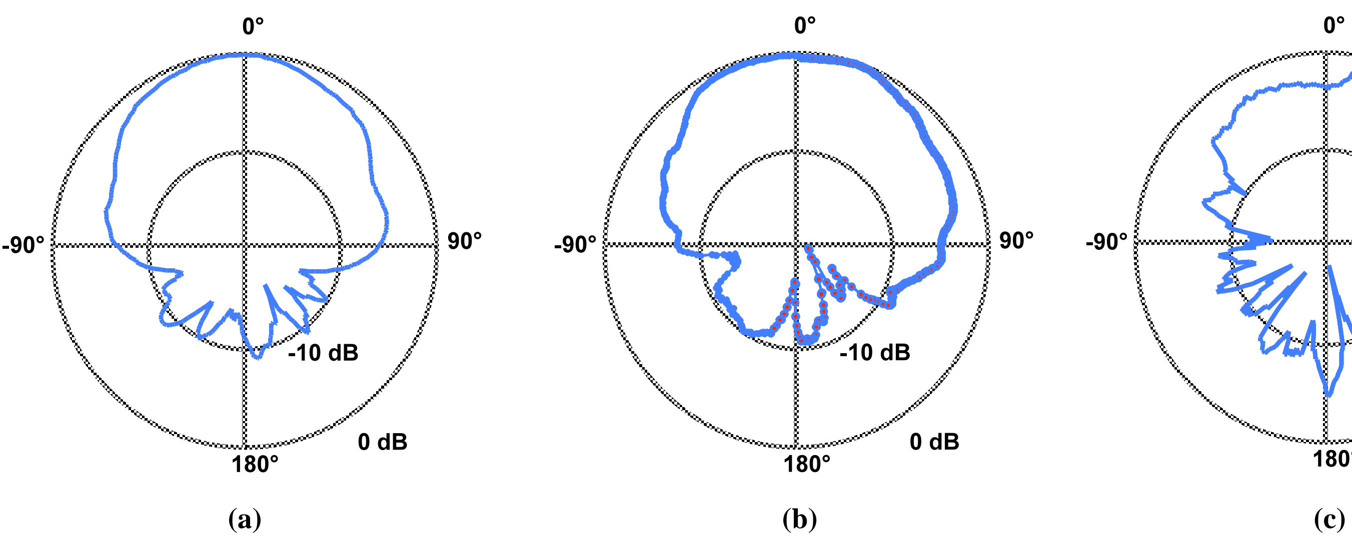

Figure 54: Radiation patterns of MEMS-tuned antenna at (a) 5.085 GHz, (b) 5.890 GHz, and (c)

Future Work

The work presented here validates the ability of MEMS variable inductors to serve as reactive loads in tunable patch antenna designs. However, the true advantage of introducing MEMS variable inductors to the art of tunable antennas is in combining MEMS inductors with MEMS capacitors in variable networks with multiple degrees of freedom. Such networks could require smaller tuning ranges for each individual component while achieving frequency shifts greater than that which can be achieved by one device alone.

An example of such a network would be the L network, which consists of a component in series and another in parallel. An L network consisting of a series inductor and a shunt capacitor is shown in Figure 55.

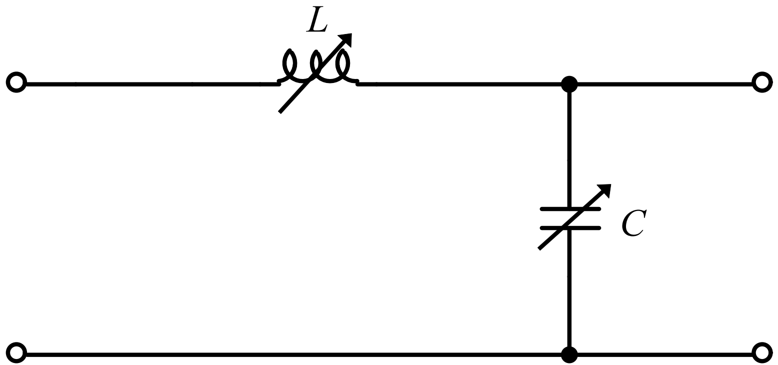

Figure 55: L network circuit diagram

Figure 56 displays Sonnet™ simulation results for the L network shown in Figure 55 modeled as ideal components and coupled to a microstrip patch antenna.

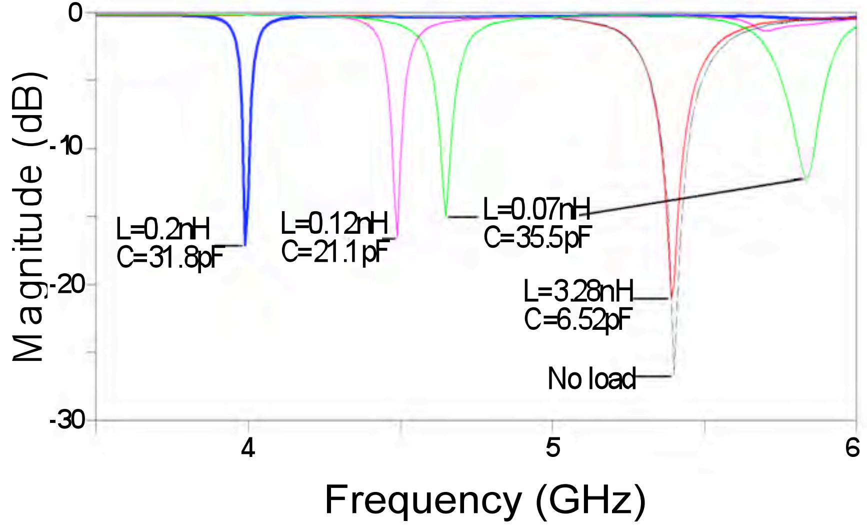

Figure 56: Simulated return loss of rectangular patch antenna loaded with variable L network

Simulated frequency shifts shown in Figure 56 span from 3.98 GHz to 5.8 GHz for variable inductances L from 0.07 nH and 0.2 nH and for variable capacitances C from 21.1 pF to 35.5 pF. This represents a bandwidth of 33.2% relative to the unloaded resonant frequency of 5.45 GHz.

Another possible matching network is the Π network, which consists of three reactive components, two arranged in shunt separated by the other in series as shown in Figure 57 with two shunt capacitors and one series inductor.

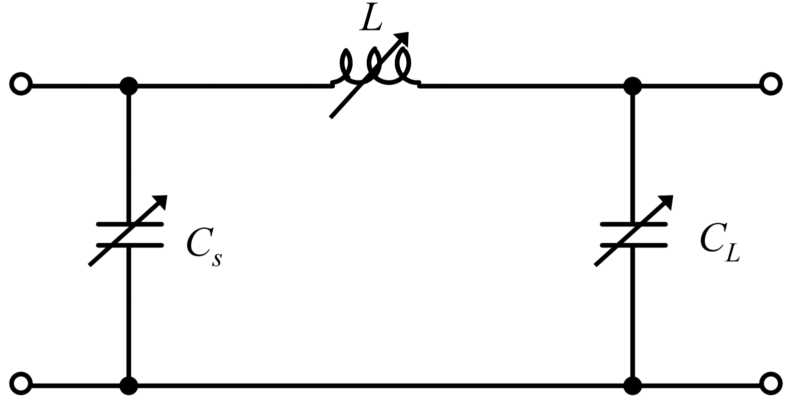

Figure 57: Circuit diagram of Π network load

By adding a third degree of freedom to patch antenna loads via a Π network of variable components, required tuning ranges for the individual components are reduced. Sonnet™ simulations of the network shown in Figure 57 modeled with ideal components and coupled to a rectangular microstrip patch antenna are shown in Figure 58.

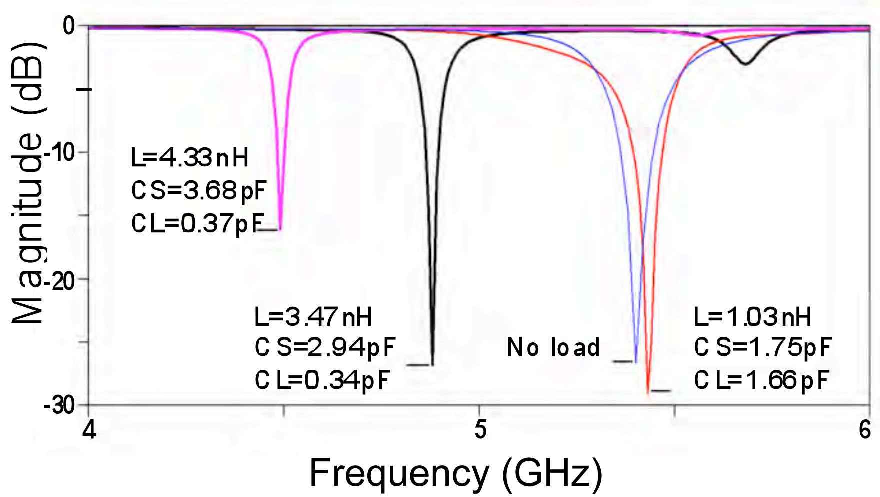

Figure 58: Simulated return loss rectangular patch antenna loaded with variable Π network

From Figure 58, one observes that the resonant frequency shifts down to 4.5 GHz and upwards to almost 5.5 GHz for capacitance *Cs* from 1.75 to 3.68 pF, inductance L from 1.03 to 4.33 nH, and capacitance *CL* of 0.34 to 1.66 pF. This represents an 18% bandwidth from the unloaded center frequency of 5.45 GHz.

Because the MEMS inductors and capacitors presented here are co-fabricated in the same process, they have the potential to be combined into effective variable networks with multiple degrees of freedom on a single die. Such a device is not yet fully explored but is offered as a future direction in tunable patch antenna design that builds on the MEMS variable inductor work described here.

Conclusions

The reactive loading tuning concept was validated using discrete surface mount inductors and capacitors to effectively tune the operating frequency of microstrip patch antennas. The rectangular patch antennas were designed for 5.5 GHz natural resonant frequencies using well-known antenna design equations. Observed shifts in the operating frequency proved the validity of the reactive loading method.

MEMS inductors and capacitors were designed, packaged, and tested as variable reactive loads in antenna tuning applications. Fabricated through the MetalMUMPs process, the components featured thermal and electrostatic actuation, respectively. Both components achieved variable reactance through mechanical motion induced by applied bias voltage.

Then, a proof of concept 5 GHz MEMS inductor-tuned patch antenna was successfully designed, fabricated, and tested, achieving an 810 MHz upward operating frequency shift, a 40 MHz continuous tuning range, and a second resonant mode at 7.85 GHz. This antenna represents a novel tuning method, demonstrating the validity of using MEMS variable inductors as variable reactive loads.

Finally, future work on tunable antennas using variable networks featuring MEMS inductor and capacitor combinations was proposed. Such designs can leverage multiple degrees of freedom to achieve wider frequency shifts with smaller individual device tuning ranges. Because the MEMS designs presented here are co-fabricated in the same process, they have potential to realize these variable network loads and dramatically deepen the art of tunable antenna design.

References

[1] C.A. Balanis, Antenna Theory: Analysis Design, Third Edition, John Wiley & Sons, Inc. (Hoboken, New Jersey), 2005, pp.811–872.

[2] J.T. Bernhard, Reconfigurable Antennas, Morgan & Claypool Publishers, (University of Illinois at Urbana–Champaign), 2007, pp. 1–53.

[3] N. Haridas, A. Drdogan, T. Arslan, A. Walton, S. Smith, T. Stevenson, C. Dunare, A. Gundlach, J. Terry, P. Argyrakis, K. Tierney, A. Ross, T. O'Hara, Reconfigurable MEMS Antennas, *Proceedings of the 2008 NASA/ESA Conference on Adaptive Hardware and Systems,* 22–25 June 2008, pp. 147–154.

[4] E. Erdil, K. Topalli, M. Unlu, O.A. Civi, T. Akin, Frequency Tunable Microstrip Patch Antena Using RF MEMS Technology, *IEEE Transactions on Antennas and Propagations, Vol. 55, Issue 4,* April 2007, pp. 1193–1196.

[5] R.J. Langley, H.J. Lee, L. Liu, K.L. Ford, Tunable Antennas and Band Gap Surfaces, *Adaptable and Tunable Antenna Technology for Handsets and Mobile Computing Products, 2009 IET Seminar*, 22 October 2009, pp. 1–34.

[6] K. Topalli, E. Erdil, O.A. Civi, Reconfigurable Antennas Using MEMS Technology, *28th General Assemply of URSI,* 23–29 October 2005, pp. 1–4.

[7] I. Zine El-Abidine and M. Okoniewski, A tunable radio frequency MEMS inductor using MetalMUMPS, *Journal of Micromechanics and Microengineering, Vol. 17,* October 2007, pp. 2280–2287.

[8] T. Yammouch, K. Okada, K. Masu, Physical Modeling of MEMS Variable Inductor, IEEE Transactions on Circuits and Systems – 11: Express Briefs, Vol. 55, Issue 5, May 2008, pp. 419–422.

[9] Z. El-Abidine, M. Okoniewski, J.G. McRory, A Tunable RF MEMS Inductor, *Proceedings of the 2004 International Conference on MEMS, NANO and Smart Systems*, 24–27 July 2005, pp. 436–437.

[10] Y. Mizuochi, S. Amakawa, N. Ishihara, K. Masu, Study of air-suspended RF MEMS inductor configurations for realizing large inductance variations, *Proceedings of the Argentine School of Micro-Nanoelectronics, Technology and Applications 2009*, 1–2 October 2009, pp. 50–55.

[11] W.L. Stutzman, G.A. Thiele, Antenna Theory and Design, Second Edition, John Wiley & Sons, Inc. (Hoboken, New Jersey), 1998, pp. 1–224.

[12] J.G. Lee, *The Effects of VSWR on Transmitted Power*, www.antennex.com/preview/vswr.htm, accessed 02 May 2011.

[13] C.K. Alexander, M.N.O. Sadiku, Fundamentals of Electric Circuits, Fourth Edition, The McGraw-Hill Companies, Inc. (New York, New York), 2009, pp. 369–412.

[14] B.C. Wadell, Transmission Line Design Handbook, Artech House, Inc. (Norwood, MA), 1991, pp. 9–478.

[15] F.T. Ulaby, Fundamentals of Applied Electromagnetics, Prentice Hall, Inc. (Upper Saddle River, New Jersey), 2010.

[16] A. Cowen, B. Dudley, E. Hill, M. Walters, R. Wood, S. Johnson, H. Wynands, B. Hardy, *MetalMUMPs Design Handbook; a MUMPs® process*, MEMScAP, Inc., 2002.

[17] Rebeiz, Gabriel M. RF MEMS: Theory, Design, and Technology, John Wiley & Sons, Inc. (Hoboken, New Jersey), pp. 22-57.

Appendix A: Patch Antenna Dimension Calculation

```
% Approximation Program - Patch Antenna
% Steven C. Yee
% 04AUG10

%% Clear everything.
clc;
clear all;
close all;
%% Initialize constants
% meters to mils conversion
milpermet = 39370.0787;

% permeability constant
mu_0 = pi*4e-7;         % H/m
% mu_0 = mu_0/39370.0787; % H/mil

% permittivity constant
e_0 = 8.85e-12;         % F/m
% e_0 = e_0/39370.0787;   % F/mil

% speed of light
c = 3e8; % m/s;

% impedance of free space
Z_free = 1/(c*e_0);

%% Specify parameters
% Input operating frequency here.
fo = 5.5e9; % Hz

% Free space wavelength in meters
lamda = c/fo;

% Height of the substrate in mils.
h = 30;     % mils
h = h/milpermet; % meters

% Relative dielectric constant of substrate (ULTRALAM2000)
erel = 2.5;

% Thickness of copper in mils
t_mil = 1.4;
t = t_mil/milpermet;

% Desired characteristic impedance in ohms
Zo = 50;

% Wavenumber in free space
ko = 2*pi/lamda;
```

```
%% Width calculation
% Width of patch in meters
W = (c/(2*fo))*sqrt(2/(erel + 1));

%% Effective dielectric constant calculation
ereff = (erel + 1)/2 + ((erel -1)/2)*((1 + 12*(h/W))^(-0.5));

%% L calculation
% L offset
Ldelt = (h*0.412*(ereff + 0.3)*(W/h + 0.264))/...
    ((ereff - 0.258)*((W/h) + 0.8));

% True length
L = 1/(2*fo*sqrt(ereff*mu_0*e_0))-2*Ldelt;

%% Effective electrical length (for reference)
Leff = L + 2*Ldelt;

%% Calculation of the input resistance of the antenna
% Calculate the admittance of a slot
 if h/lamda < 1/10
     G1 = (W/(120*lamda))*(1-(1/24)*(ko*h)^2);
     B1 = (W/(120*lamda))*(1 - 0.636*log(ko*h));
 end

% Set an integration resolution of 1000 for a Riemann Sum operation.
res = 1e3;
% Limits of integration
theta = 0:pi/res:pi- pi/res;
% Evaluate the integral
inside_int = (sin((ko*W.*cos(theta)/2))./...
    cos(theta)).^2.*besselj(0, ko*L.*sin(theta)).*sin(theta).^3;
% Apply Reimann Sum width. (integrate)
int = sum(inside_int)*(pi/res);

% Cpmplete the expression for mutual admittance
G12 = (1/(120*pi^2))*int;
% Calculate the real impedance for both odd and even mode waves.
Rin_mut = 1/(2*(G1 - G12));
Rin_mutup = 1/(2*(G1 + G12));
% Calculate the average of the impedances for the edge input impedance
% Z_in_ant = (Rin_mut + Rin_mutup)/2; % theoretical - from Balanis
Z_in_ant = 90.*(L./W).^2*(erel.^2)./(erel - 1); % simulation and from
Stutzman

%% Input feedline width
% Initial feedline width needed to achieve 50 ohm port matching condition
W_feed = (((5.98*h)/(exp(sqrt(ereff + 1.41)*Zo/87))) - t)/0.8;

%% Input feedline capacitance in pF/in
C_feed_in = 0.67*(ereff + 1.41)/log(5.98*h/(0.8*W + t));

%% 1/4 wavelength transformer width
```

```
% Impedance of the 1/4 wavelength transformer
Z_transform = sqrt(Zo*Z_in_ant);

% Width needed to achieve above impedance
W_transform = (((5.98*h)/...
    (exp(sqrt(ereff + 1.41)*Z_transform/87))) - t)/0.8;

%% 1/4 wavelength transformer length
% 1/4 wavelength in the dielectric material in meters
L_transform = (1/(fo*sqrt(ereff*e_0*mu_0)))*0.25;

%% 1/4 wavelength transformer capacitance in pF/in
C_transform_in = 0.67*(ereff + 1.41)/log(5.98*h/(0.8*W_transform + t));

%% Convert all units to mils
L_mil = L*milpermet;
W_mil = W*milpermet;
Leff = Leff*milpermet;
h_mil = h*milpermet;
W_feed_mil = W_feed*milpermet;
W_transform_mil = W_transform*milpermet;
L_transform_mil = L_transform*milpermet;

%% Other unit conversions
% Capacitance of input feed in pF/mil
C_feed_mil = C_feed_in/1000;

% Capacitance of input feed in pF/m
C_feed_met = C_feed_mil*milpermet;

% Capacitance of 1/4 wave transform in pF/mil
C_transform_mil = (C_transform_in/1000);

% Capacitance of 1/4 wave transform in pF/m
C_transform_met = C_transform_mil*milpermet;

% Capacitance of 1/4 wave transform total
C_trans_tot = C_transform_met*L_transform;

%% Using an inset feed instead of a quarter wavelength transformer.
% Calculate the impedance of the transmission line assuming that the
% previous calculation for a 50 ohm characteristic impedance microstrip
% line is correct.
if W_feed/h < 1
    Z_ch = (60/sqrt(ereff))*log(8*h/W_feed + W_feed/(4*h));
end
if W_feed/h == 1
    Z_ch = (60/sqrt(ereff))*log(8*h/W_feed + W_feed/(4*h));
end
if W_feed/h > 1
    Z_ch = 120*pi/(sqrt(ereff)*((W_feed/h) + 1.393 + 0.667*...
        log((W_feed/h + 1.444))));
end
```

```
% The result returned is 50.3471 ohms, which I will take as close
% for this approximation program.

% Calculate the inset distance.
y_inset = acos(sqrt(50/Z_in_ant))*L/pi;
% Convert the inset distance to mils.
y_inset_mil = y_inset*milpermet;

%% Display the relevant information
L_mil
W_mil
h_mil
W_feed_mil
W_transform_mil
L_transform_mil
y_inset_mil
Z_in_ant
Z_transform

%% Calculuate input reactance and resistance as a function of frequency
f_test = 6e9:0.01e9:12e9; %range of test frequencies 1-20 GHz
lamda_test = c./f_test; %calculate free space wavelengths
ko_test = 2.*pi./lamda_test; % calculate wave numbers
B1_susceptance = (W./(120.*lamda_test)).*(1 - 0.636.*log(ko_test.*h)); %
calculate the slot susceptance
G1_admittance = (W./(120.*lamda_test)).*(1-(1/24).*(ko_test.*h).^2); %
calculate the slot admittance
X1_reactance = 1./B1_susceptance; % calculate the slot reactance
R1_resistance = 1./G1_admittance; % calculate the slot resistance
Z1 = R1_resistance + 1i.*X1_reactance; % calculate the slot impedance
(complex)
Y1 = 1./Z1;
Z2 = Z1; % slot 1 equals slot 2
if W/h > 1
    Z_char_ant = 120*pi/(sqrt(ereff)*((W/h) + 1.393 + 0.667*...
        log((W/h + 1.444))));
end % calculates the characteristic impedance of the patch
Beta = 2*pi./lamda_test; %calculates beta
Z2_prime = Z_char_ant.*((Z2 + 1i.*Z_char_ant.*tan(Beta.*L))./...
    (Z_char_ant + 1i.*Z2.*tan(Beta.*L))); %transformation eqn.
Y2_prime = 1./Z2_prime; %Y2 transformed to input
Y_in = Y1 + Y2_prime; % total admittance (add in parallel)
Z_in_test = 1./Y_in; % total input resistance
R_in_test = real(Z_in_test); % real input resistance
X_in_test = imag(Z_in_test); % imag input reactance

figure(1) % plot the input resistance and reactance as functions of
frequency.
subplot(2,1,1), plot(f_test/1e9, R_in_test), title('Input Resistance v.
Frequency'),...
    xlabel('Frequency (Ghz)'), ylabel('Resistance (ohms)'), grid on;
subplot(2,1,2), plot(f_test/1e9, X_in_test), title('Input Reactance v.
Frequency'),...
    xlabel('Frequency (GHz)'), ylabel('Reactance (ohms)'), grid on;
```

Appendix B: Microstrip Line Width Calculation

```
%% Initialize constants
% meters to mils conversion
milpermet = 39370.0787;
 % permeability constant
mu_0 = pi*4e-7;         % H/m
% mu_0 = mu_0/39370.0787; % H/mil
 % permittivity constant
e_0 = 8.85e-12;         % F/m
% e_0 = e_0/39370.0787;   % F/mil
 % speed of light
c = 3e8; % m/s;
 % impedance of free space
Z_free = 1/(c*e_0);
 %% Input feedline width (assume greater than 30 mils wide)
% Initial feedline width needed to achieve 50 ohm port matching condition
 erel = 2.94;
h = 30;
t = 1.4;
 w = (30:300);
e_eff = ((erel + 1)/2) + ((erel-1)/2).*(1 + 12*h./w).^-0.5;
w_prime = w + t.*((1 + 1./e_eff)./(2.*pi)).*...
    log(4.*exp(1)./sqrt((t./h).^2 + ((1./pi).*(1./((w./t) + 11/10))).^2));
 Z_line_thick = (Z_free./(2.*pi.*...
    sqrt(2*(e_eff + 1)))).*log(1 + (4*h./w_prime).*...
    (((14 + (8./e_eff))./11).*4.*h./w_prime + ...
    sqrt(((14 + (8./e_eff))./11).^2.*(4.*h./w_prime).^2 +...
    ((1 + (1./e_eff)).*pi.^2./2))));
 figure(1)
plot(w, Z_line_thick), ylabel('Ch. Impedance (OHMS)'), ...
    xlabel('Width (mils)'), title('Z characteristic for w/h >1'),...
    grid on;
 w2 = (1:30);
e_eff2 = ((erel + 1)/2) + ((erel-1)/2).*((1 + 12*h./w2).^-0.5 + ...
    0.04*(1 - w2./h).^2);
w_prime2 = w2 + t.*((1 + 1./e_eff2)./(2.*pi)).*...
    log(4.*exp(1)./sqrt((t./h).^2 + ((1./pi).*(1./((w2./t) + 11/10))).^2));
 Z_line_thin = (Z_free./(2.*pi.*...
    sqrt(2*(e_eff2 + 1)))).*log(1 + (4*h./w_prime2).*...
    (((14 + (8./e_eff2))./11).*4.*h./w_prime2 + ...
    sqrt(((14 + (8./e_eff2))./11).^2.*(4.*h./w_prime2).^2 +...
    ((1 + (1./e_eff2)).*pi.^2./2))));
figure(2)
plot(w2, Z_line_thin), ylabel('Ch. Impedance (OHMS)'), ...
    xlabel('Width (mils)'), title('Z characteristic for w/h < 1'),...
    grid on;
```

Appendix C: MetalMUMPs [16]

1.3. MetalMUMPs Process Flow

Oxide 1 Deposited

FIGURE 1.2. A 2μm thick oxide (Isolation Oxide) is grown on the surface of the starting n-type (100) silicon wafer. This is followed by deposition of a 0.5μm thick sacrificial phosphosilicate glass (PSG) layer (Oxide 1).

Oxide 1 Patterned — **Mask Level: OXIDE1**

FIGURE 1.3 The wafers are coated with UV-sensitive photoresist and lithographically patterned by exposing to UV light through the first level mask (OXIDE1), and then developing it. The photoresist in exposed areas is removed, leaving behind a patterned photoresist mask for etching. Wet chemical etching is used to remove the unwanted sacrificial PSG. After the etch, the photoresist is chemically stripped. This method of patterning the wafers with photoresist, etching and stripping the remaining photoresist is used repeatedly in the MetalMUMPs process.

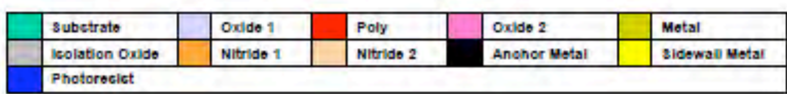

Nitride 1 and Poly Deposited

FIGURE 1.4. A 0.35µm layer of silicon nitride (Nitride 1) is deposited, followed immediately by the deposition of a 0.7µm layer of polysilicon (Poly).

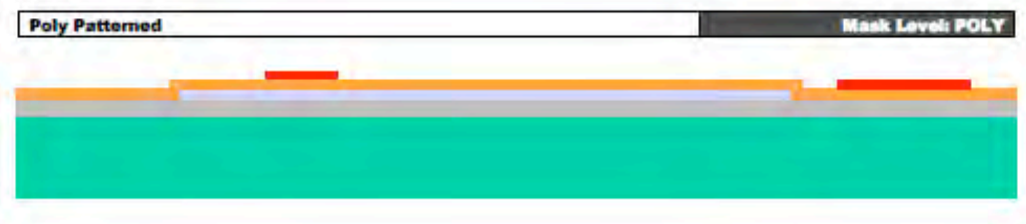

FIGURE 1.5. The wafers are coated with photoresist and the second level (POLY) is lithographically patterned. Reactive ion etching (RIE) is used to remove the unwanted polysilicon. After the etch is completed, the photoresist is removed.

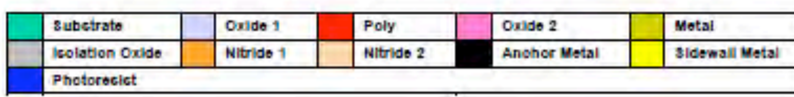

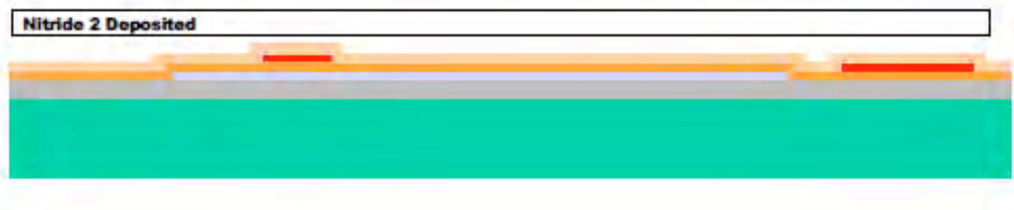

FIGURE 1.6. A second 0.35µm layer of silicon nitride (Nitride 2) is deposited.

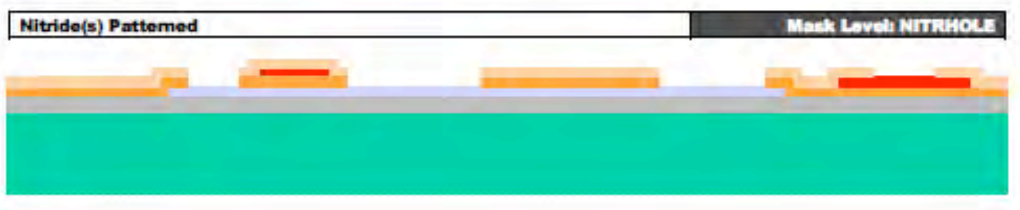

FIGURE 1.7. The wafers are coated with photoresist and the third level (NITRHOLE) is lithographically patterned. RIE etching is performed to remove both Nitride 2 and Nitride 1 from the patterned areas. After the etch is complete, the photoresist is removed. Note: Nitride 1 will remain anywhere NITRHOLE is patterned over Poly.

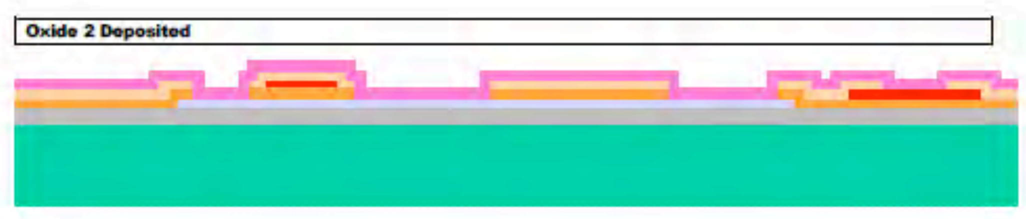

FIGURE 1.8. A second sacrificial layer (Oxide 2), 1.1µm of PSG, is deposited and annealed at 1050°C for 1 hour.

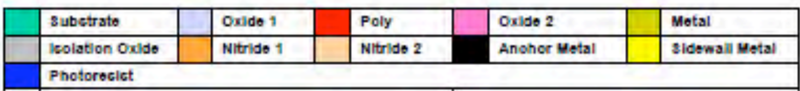

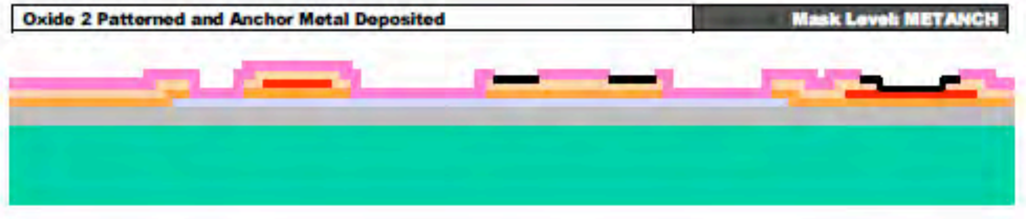

FIGURE 1.9. The wafer is coated with photoresist and the fourth mask level (METANCH) is lithographically patterned. The Oxide 2 is wet etched and a thin metal layer (Anchor Metal) consisting of 10nm Cr + 25nm Pt is deposited. A liftoff process is used to remove the photoresist and leave Anchor Metal only in the bottom of the Oxide 2 openings formed from the METANCH mask level.

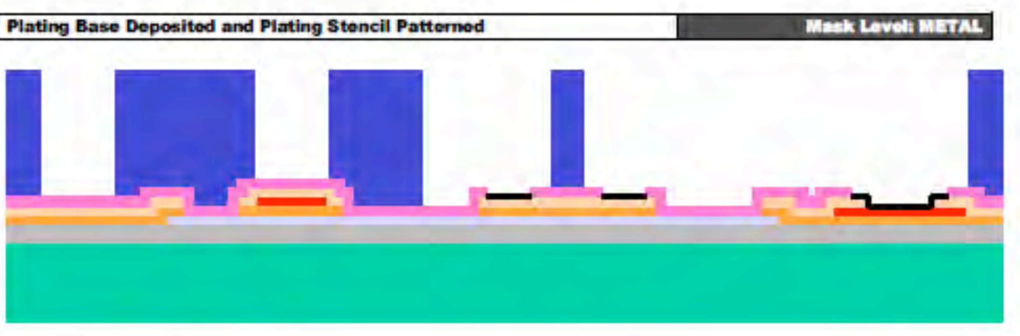

FIGURE 1.10 The Plating base layer, consisting of 500nm Cu + 50nm Ti is deposited. (Not shown). The wafers are coated with a thick layer of photoresist and patterned with the fifth mask level (METAL). This process forms a patterned stencil for the electroplated Metal layer.

	Substrate		Oxide 1		Poly		Oxide 2		Metal
	Isolation Oxide		Nitride 1		Nitride 2		Anchor Metal		Sidewall Metal
	Photorecict								

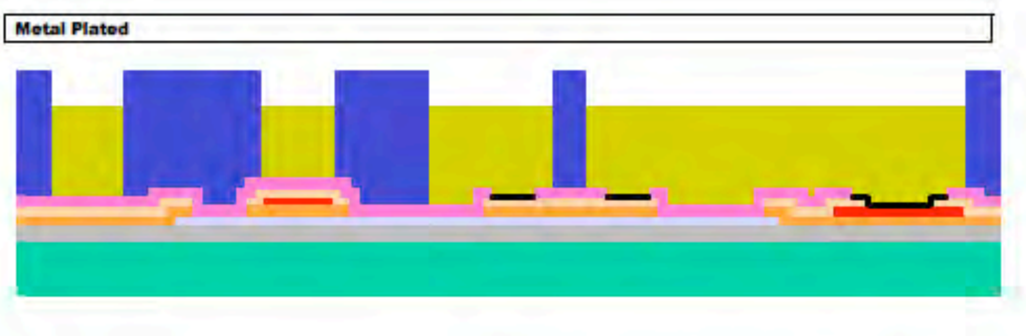

FIGURE 1.11. Nickel is electroplated to a nominal thickness of 20μm into the patterned resist stencil. A 0.5μm gold layer is then immediately electroplated on top of the nickel layer. This forms the Metal layer.

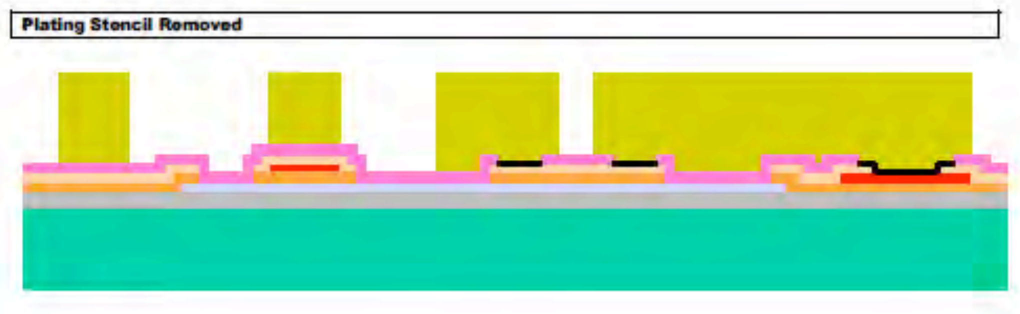

FIGURE 1.12. The photoresist stencil is then chemically removed.

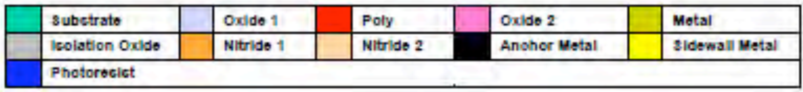

FIGURE 1.13. The wafers are coated with photoresist and patterned with a "bloated" version of the sixth mask level (GOLDOVP) to remove Plating Base in the regions where Sidewall Metal is desired. The Plating Base is chemically removed from the unpatterned regions, and the photoresist is stripped. The wafers are coated with photoresist and patterned with an "un-bloated" version of the sixth mask level (GOLDOVP) to define a resist stencil in the regions of Metal where electroplated Sidewall Metal is desired.

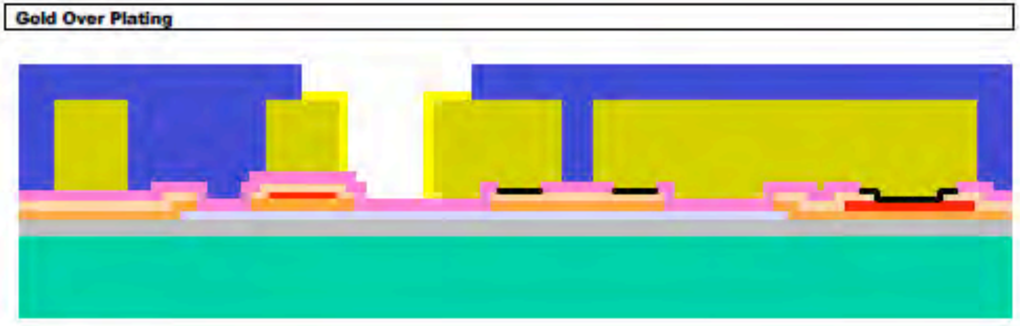

FIGURE 1.14. A 1-3µm gold layer (Sidewall Metal) is electroplated using the GOLDOVP photoresist mask as a stencil.

Substrate	Oxide 1	Poly	Oxide 2	Metal
Isolation Oxide	Nitride 1	Nitride 2	Anchor Metal	Sidewall Metal
Photoresist				

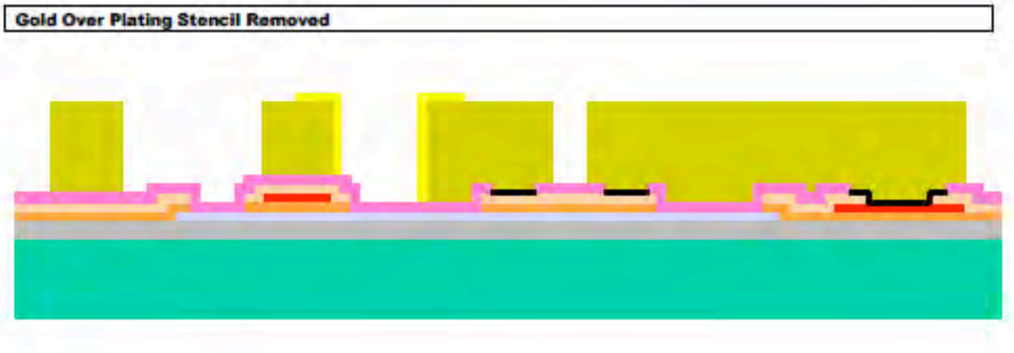

FIGURE 1.15. The GOLDOVP resist stencil is stripped.

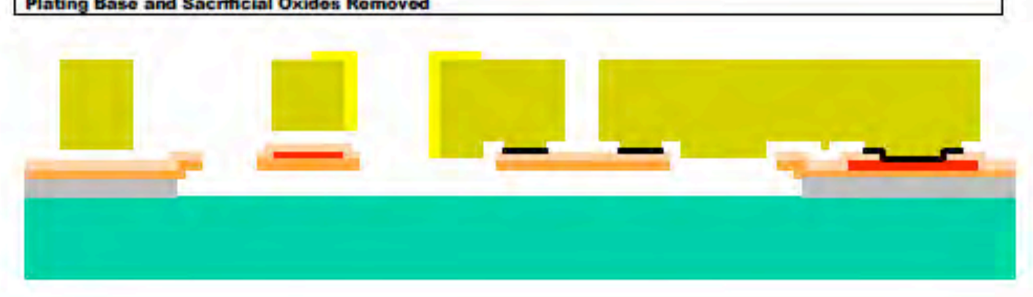

FIGURE 1.16. Plating Base is chemically stripped in the first step of the release process. In the second step of the release process, a 49% HF solution is used to remove the PSG sacrifical layers (Oxide 1 and Oxide 2) and the Isolation Oxide layer over the trench areas.

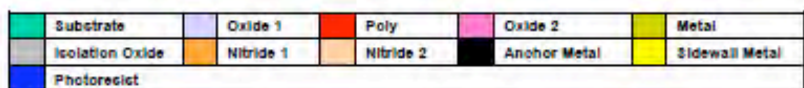

Trench Formed (Silicon Etched)

FIGURE 1.17. In the final step of the release process, a KOH silicon etch is used to form a 25µm deep trench in the silicon substrate in the areas defined by the OXIDE1 and NITRHOLE mask levels.

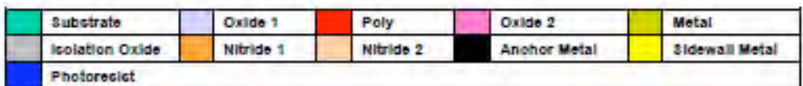

Appendix D: MetalMUMPs Mask Layout